

The disappearance of a massive star marking the birth of a black hole in M31

Kishalay De^{1*}, Morgan MacLeod², Jacob E. Jencson³, Elizabeth Lovegrove⁴,
Andrea Antoni⁵, Erin Kara¹, Mansi M. Kasliwal⁶, Ryan M. Lau⁷, Abraham Loeb^{2,8},
Megan Masterson¹, Aaron M. Meisner⁷, Christos Panagiotou¹, Eliot Quataert⁹
and Robert Simcoe¹

¹ Kavli Institute for Astrophysics and Space Research, Massachusetts Institute of Technology, Cambridge,

MA 02139, USA

² Center for Astrophysics — Harvard & Smithsonian 60 Garden Street, MS-16, Cambridge, MA 02138, USA

³ IPAC, Mail Code 100-22, Caltech, 1200 E. California Blvd., Pasadena, CA 91125

⁴ United States Naval Observatory

⁵ Center for Computational Astrophysics, Flatiron Institute, New York, NY 10010, USA

⁶ Cahill Center for Astrophysics, California Institute of Technology, 1200 E. California Boulevard, Pasadena,
CA 91125, USA

⁷ NSF's National Optical-Infrared Astronomy Research Laboratory, 950 N. Cherry Ave., Tucson,
AZ 85719, USA ⁸ Black Hole Initiative, Harvard University, Cambridge, MA 02138, USA

⁹ Department of Astrophysical Sciences, Princeton University, Princeton, NJ 08544, USA

*Corresponding author. Email: kde1@mit.edu

Stellar mass black holes are formed from the terminal collapse of massive stars if the ensuing neutrino shock is unable to eject the stellar envelope. Direct observations of black hole formation remain inconclusive. We report observations

of M31-2014-DS1, a massive, hydrogen-depleted supergiant in the Andromeda galaxy identified via a mid-infrared brightening in 2014. Its total luminosity remained nearly constant for the subsequent thousand days, before fading dramatically over the next thousand days by $\gtrsim 10\times$ and $\gtrsim 10^4\times$ in total and visible light, respectively. Together with the lack of a detected optical outburst, the observations are explained by the fallback of the stellar envelope into a newly formed black hole, moderated by the injection of a $\sim 10^{48}$ erg shock. Unifying these observations with a candidate in NGC 6946, we present a concordant picture for the birth of stellar mass black holes from stripped massive stars.

When massive ($\gtrsim 10 M_\odot$) stars run out of nuclear fuel, they collapse into their cores (1, 2), commonly followed by energetic ($\sim 10^{51}$ erg) and luminous ($\gtrsim 10^7 L_\odot$) core-collapse supernovae explosions leading to birth of neutron stars (3, 4). A stellar mass black hole (BH) may form if some or all of the envelope fails to be ejected (5, 6). Although nominally failed, the loss of gravitational binding energy (equivalent to $\approx 0.2 - 0.5 M_\odot$) via neutrino emission (5, 7) and feedback from inefficient accretion (8–12) have been predicted to inject $\sim 10^{45} - 10^{49}$ erg into the outermost, loosely bound stellar envelope. While most of the star falls into the newly-formed BH, some of this envelope may become unbound, possibly resulting in a faint ($\lesssim 10^6 L_\odot$), year-long optical outburst (13–15). In the aftermath, the remnant would become enshrouded in a dusty envelope (16). Despite presenting a critical missing link between stellar progenitors and their remnant BHs, the challenging task of identifying individual disappearing stars at extragalactic distances, together with the faint luminosity of the optical outburst (if any), has limited the identification and consistent interpretation of such ‘failed supernovae’.

The disappearance of a massive supergiant in M31

Using a new image subtraction pipeline (17) for data from the NEOWISE (18, 19) mid-infrared (MIR) sky survey, we searched for MIR outbursts in the direction of the Andromeda (Messier 31) galaxy (Materials and Methods). We identified a faint MIR brightening of a star (internally cataloged as WTP 16aathhy; hereafter M31-2014-DS1) at celestial J2000 coordinates $\alpha = 00:45:13.47$, $\delta = +41:32:33.14$ (Materials and Methods; Figure 1). The source increased in MIR flux by $\approx 50\%$ over

≈ 2 years starting in 2014, subsequently fading below the progenitor flux within the next ≈ 1 year and continuing to fade until 2022 (Figure 1). It simultaneously faded dramatically (by $\gtrsim 100\times$) in optical light between 2016 and 2019, and was undetected in recent deep optical and near-IR (NIR) imaging observations using the MMT and IRTF telescopes in 2023 (Materials and Methods; Figure 1).

The optical counterpart of the progenitor was previously identified as an irregular variable star (20) (as confirmed with its variable optical brightness between 2010 and 2014; Figure 1), and recently suggested to be a candidate red supergiant (RSG) in M31 based on its brightness and colors (21). Using archival data from the Hubble Space Telescope (HST) and Spitzer Space Telescope (SST) taken between 2008 and 2012, we model the complete Spectral Energy Distribution (SED; Materials and Methods) incorporating a warm dust shell surrounding the progenitor star to account for the flat spectrum extending to MIR bands (Figure 2). The analysis constrains the progenitor star to be a luminous ($\log(L/L_\odot) \approx 5$) and cool ($T_{\text{eff}} \approx 4500$ K) supergiant, surrounded by a dust shell with a temperature of ≈ 870 K at a radius of ≈ 110 AU. While the progenitor is hotter than the nominal end-point of single star evolutionary tracks in the MIST database (22), the source appears similar (Figure 2) to progenitors of some known H-deficient supernovae (SNe (4)), suggested to arise from enhanced terminal mass loss (23, 24) removing most of the stellar H-envelope. Therefore, we construct a suite of stellar models (25) with enhanced wind mass loss (Materials and Methods), and find the progenitor to be consistent with a star born with an initial mass of $\approx 20 M_\odot$ that reaches its terminal nuclear burning phase with a mass of $\approx 6.7 M_\odot$ and a thin $\approx 0.55 M_\odot$ H envelope (Figure 2).

Analyzing serendipitous HST observations of the field from 2022 (≈ 8 years after the start of the MIR brightening), we find the source to be undetected in the visual F606W filter, but an extremely faint source ($\gtrsim 10^4\times$ fainter than the progenitor) is detected in the redder F814W filter. We obtained NIR imaging and spectroscopy of the IR remnant in 2023 using the Keck-I and Keck-II telescopes respectively. The data confirm a faint NIR remnant (Figure 1) exhibiting a steep red spectrum (Figure 3) brightening to longer wavelengths, consistent with detection in recent NEOWISE data. By modeling the remnant SED, we find the source to be currently obscured behind an optically thick (optical depth $\tau \gtrsim 20$) dust shell, while its bolometric luminosity and effective radius has decreased to $\lesssim 10\%$ and $\lesssim 20\%$ of the progenitor respectively (Figure 3, Materials and Methods).

To empirically understand the nature of the dimming, we model the temporal evolution of the central star and circumstellar dust shell using the contemporaneous optical coverage from Gaia (26) and MIR coverage from NEOWISE. The best-fit models reveal a nearly constant bolometric luminosity in the first ≈ 1000 days since the start of the MIR brightening, followed by a decline by $\approx 10\times$ over the next ≈ 1000 days (Materials and Methods; Figure 4). The MIR brightening can be attributed to emission from new, hot dust (≈ 1300 K) formed well inside the progenitor dust shell, that causes the effective inner radius to recede to the minimum distance at which dust can form given the luminosity of the source (the dust condensation radius; $r_c \approx 30$ AU. Materials and Methods). The formation of this same dust shell results in a $\approx 10\times$ increase in the dust optical depth, causing the dramatic optical fading, while enshrouding the source in an additional $\approx 10^{-4} M_\odot$ of dust (Materials and Methods). Despite evidence for a new dust shell likely caused by an impulsive mass ejection, we find no evidence of an associated optical outburst exceeding the characteristic stellar variability in the extensive pre-fading photometric coverage (Figure 1). We conservatively constrain the luminosity and duration of a possible missed outburst to $\lesssim 10^5 L_\odot$ and $\lesssim 70$ d, respectively (Materials and Methods).

The collapse of the stellar core

The dramatic and sustained fading of M31-2014-DS1 is exceptional in the landscape of variability in massive, evolved stars (27, 28). While enhanced mass loss episodes in H-rich RSGs have been predicted theoretically to cause optical dimmings (29, 30), H-depleted stars like M31-2014-DS1’s progenitor brighten instead when they contract upon losing mass (31). Similarly, temporary optical fadings due to increased dust obscuration have been observed among massive stars, but are distinct from the simultaneous and long-term optical, infrared and bolometric fading seen in M31-2014-DS1 (32, 33). The sudden decline of luminosity in M31-2014-DS1 points to the cessation of nuclear burning together with a subsequent shock that fails to overcome the infalling material; lacking any evidence for a luminous outburst at such proximity, the observations of M31-2014-DS1 bespeak signatures of a ‘failed’ SN that leads to the collapse of the stellar core. Based on analytical models for outbursts powered by H recombination (34, 35), we constrain the mass of H-rich material ejected during an impulsive episode to be $\lesssim 0.03 M_\odot$ at the stellar escape velocity ($v_{esc} \approx 70$ km s $^{-1}$) and

up to $\lesssim 0.3 M_{\odot}$ and $\lesssim 1 M_{\odot}$ at $5\times$ and $25\times$ the escape velocity, respectively (Figure 4). These constraints imply that the majority of stellar material ($\gtrsim 5 M_{\odot}$) collapsed into the core, exceeding the maximum mass of a neutron star (36) (NS) and forming a BH.

We attempt to understand the in-fall of the stellar envelope following the collapse of the core noting that the free-fall time of the progenitor ($t_{ff} \approx \frac{1}{\sqrt{G\rho}} \approx 180$ d, where G is the Gravitational constant and ρ is the average stellar density), is substantially faster than the slow bolometric fading over ≈ 1000 d (Figure 4). This suggests that energy added to the outer envelope material significantly delays its fallback. To verify the effects of energy deposition, we inject our simulated H-depleted progenitor star (37) with a range of plausible outgoing shock energies ($\sim 10^{45} - 10^{49}$ erg) (7, 12, 38). During terminal stellar evolution, the same outer layers of the star are subject to vigorous convective turbulence, which carries substantial specific angular momentum (8–10) that thermalizes accretion energy (39) and suppresses direct accretion. Numerical simulations (11, 12) show that a minuscule fraction ($\lesssim 1\%$) of material falling from the outer layers of supergiant envelopes is likely to accrete directly. We adopt an analytic model for the accreted fraction based on the relative angular momentum of the inflow and the BH horizon (40) (Materials and Methods).

Comparison of our models to the data (Figure 4) suggest that the emergent luminosity is capped near (at $\approx 30 - 50\%$) the Eddington luminosity ($\approx 6 \times 10^{38}$ erg s $^{-1}$ for a $5 M_{\odot}$ BH (15)) during the extended (≈ 1000 d) luminosity plateau, even as the physical accretion rate declines rapidly. As the mass infall rate falls below the Eddington rate, the emergent luminosity becomes proportional to the accretion rate during the late decay. Larger shock energies unbind a larger fraction of the progenitor envelope, leaving behind a smaller mass that falls back over a shorter period of time. Although the exact time of the collapse is not well constrained, the $\approx 10\times$ fading over ≈ 1000 d is squarely consistent with shock energies of $10^{47} - 10^{49}$ erg (Figure 4), causing $\approx 98\%$ of the stellar mass to collapse into a $\approx 6.5 M_{\odot}$ BH.

As the weak shock ($10^{47} - 10^{49}$ erg) unbinds only $\sim 0.1 M_{\odot}$ of the outer envelope, it can produce a brief but luminous optical outburst that may be easily missed given the photometric coverage (Figure 4), consistent with our optical constraints. Noting that this ejected mass carries a distribution of velocities as it moves outwards and cools (Materials and Methods), most of the material would reach the dust condensation radius and start forming new hot dust at a characteristic timescale of $\sim r_c/v_{\text{esc}} \approx 650$ d after the ejection, consistent with the peak of the MIR brightening. Although the

details of the dust formation are sensitive to the assumed velocity distribution and dust formation process (16), given our model velocity distributions (Materials and Methods) we find that a fraction $f_{\text{shell}} \sim 0.1$ of the total ejecta lies in the hot shell near the condensation radius at a given time. The shell dust mass is therefore $m_{\text{shell}} \sim f_{\text{shell}} M_g r_{\text{dg}}$, where M_g is the total ejected gas mass ($\sim 0.1 M_{\odot}$) and $r_{\text{dg}} \approx 0.01$ is the dust-to-gas mass ratio, which indicates a characteristic mass of new dust formed of $\sim 10^{-4} M_{\odot}$, similar to that measured from the SED evolution.

A unified model for black hole formation from stripped stars

A previous candidate disappearing supergiant (named NGC 6946-BH1) was identified in the galaxy NGC 6946 (41–43), and we show its progenitor and remnant in Figures 2 and 3. Unlike M31-2014-DS1, NGC 6946-BH1 exhibited a luminous ($\sim 10^6 L_{\odot}$) optical outburst followed by an expanding dusty envelope (suggesting an impulsive ejection of $\sim 0.1 - 1 M_{\odot}$ of material (43)), making it consistent with both a failed SN from a H-rich progenitor (13) or possibly a stellar merger viewed along a dusty torus (44, 45). Particularly, it has long remained difficult to reconcile its similarly rapid bolometric fading (it faded by $\approx 10\times$ in ~ 3000 d (42)) with the long expected super-Eddington phase (~decades) of the speculated massive progenitor H-envelope (15, 43). We confirm the long timescales in our calculations by constructing a progenitor model for M31-2014-DS1 with a massive H-envelope with artificially enhanced mixing (Figure 4; Materials and Methods), consistently finding an initial Eddington limited plateau and subsequent fading timescales of $\gtrsim 10^5$ d (100 \times longer than observed).

Although the progenitor of NGC 6946-BH1 was initially identified as a likely RSG (41, 42), its nominal properties were previously suggested to be hotter than single star RSG evolutionary endpoints at the progenitor luminosity (consistent with our comparison against MIST tracks; Figure 2), and instead consistent with a yellow supergiant (46). To this end, we were also able to find a reasonable match to its hotter terminal temperature using a H-depleted star with a terminal mass of $\approx 10 M_{\odot}$ and a $\approx 1.4 M_{\odot}$ H-envelope (Figure 2; Materials and Methods). Similar to the previous analysis (Materials and Methods), the $\approx 3\times$ more massive H-envelope in this model produces a characteristic longer duration ($\sim 100 - 200$ d) H-recombination outburst as observed, together with a subsequent accretion-powered plateau and fallback timescale that is longer (~ 3000 d)

than M31-2014-DS1, but consistent with observed fading of NGC 6946-BH1 out to recent JWST observations (45, 47) (Supplementary Text).

Compared to NGC 6946-BH1, the exquisite archival data of M31-2014-DS1 owing to its membership in the nearest Milky-way like galaxy (nearly 130 years after the last known SN (48) in M31) allows us to securely relate the lack of an optical outburst and the observed fading timescale to the hydrogen depleted progenitor envelope. Therefore, drawing on the remarkable similarities between M31-2014-DS1 and NGC 6946-BH1, our analysis suggests that these objects represent an emerging class of massive stellar deaths associated with the birth of stellar mass BHs from hydrogen-depleted stars. X-ray emission from accretion onto the newly formed BHs remains currently undetected in both M31-2014-DS1 and NGC 6946-BH1, likely due to enshrouding by gas (43, 49) (Materials and Methods); however, the proximity of M31-2014-DS1 promises unique archival multi-messenger investigations in neutrinos and gravitational waves (50, 51), as well as future electromagnetic observations in the IR and X-ray bands. With theoretical predictions connecting stellar progenitors to their (possible) remnant BHs providing strikingly uncertain predictions (52, 53) and nearly no observational constraints, the terminal resemblance of the progenitor of M31-2014-DS1 to many successful SNe (Figure 2) alludes to possible chaotic dependence between stellar progenitors and their remnant compact objects as found in previous theoretical works (53, 54).

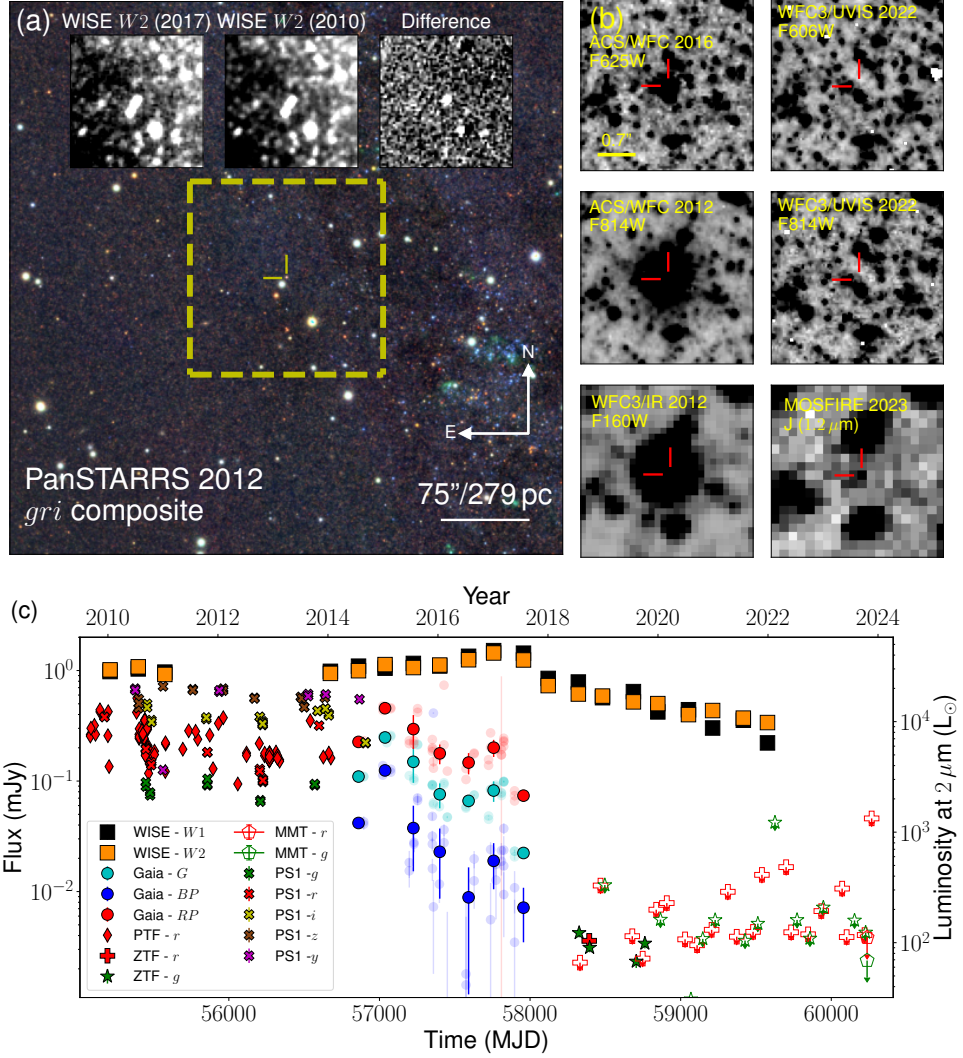


Figure 1: The discovery location, IR brightening and disappearance of M31-2014-DS1. (a) Optical color composite image of the discovery field taken from the PS1 survey (55). The image triplet in the inset shows a zoom-in (marked by the yellow dashed square) observed by the NEOWISE (18) survey in 2017 (left), 2010 (middle) and the resulting difference image (right). (b) Zoomed-in images showing the progenitor location before and $\approx 6 - 7$ years after the the MIR brightening peak. The top row shows optical data from HST, the middle row shows red optical light data from HST, and the bottom row shows near-infrared data from HST and the Keck-I telescope, highlighting the disappearance of the optical source and a very faint IR remnant. (c) The temporal evolution of flux observed with the PTF (56), NEOWISE (18), PS1 (55), Gaia (26) and ZTF (57) surveys and follow-up photometry from MMT. Error bars are shown at 1σ confidence, and 5σ upper limits are shown as hollow symbols with downward arrows. For the Gaia photometry, we show the raw flux in light symbols, while the dark symbols show the averaged flux around the NEOWISE observation epochs. The left axis indicates the brightness in units of observed flux, while the right axis shows the monochromatic luminosity (λF_λ) scaled to a mean observation wavelength of $2 \mu\text{m}$.

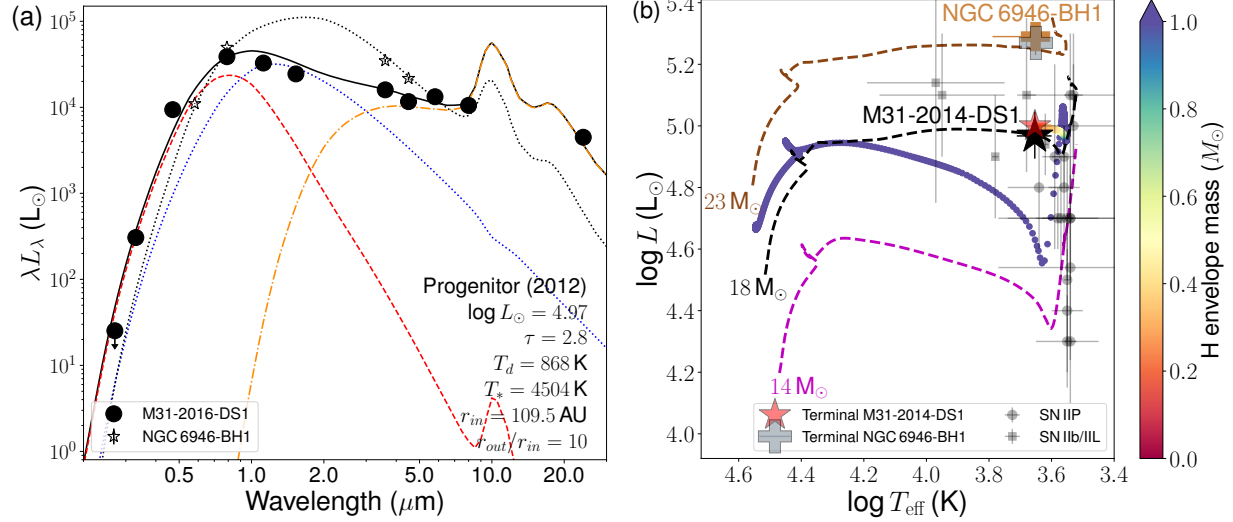


Figure 2: The spectral energy distribution and physical properties of the progenitor of M31-2014-DS1. (a) The UV to MIR SED observed with HST and SST between 2008 and 2012, along with the best-fit DUSTY model (parameters are shown). Black solid lines denote total flux, orange dot-dashed lines denote dust emission, and red dashed and blue dotted lines denote scattered and attenuated stellar emission, respectively. The SED of the progenitor of NGC 6946-BH1 (open stars) and its reported best-fit model (black dotted line) are shown. Error bars are shown at 1σ confidence, and 5σ upper limits are shown as symbols with downward arrows. (b) The luminosity and effective temperature of M31-2014-DS1 (black star) compared to single stellar evolutionary tracks at different initial masses (shown as dashed lines) from MIST (22). The progenitor of NGC 6946-BH1 (yellow plus symbol) and those of previously known hydrogen-rich SNe (58) (spectroscopic type indicated in legend) are shown. The sequence of circles shows our custom stellar evolutionary model for the progenitor of M31-2014-DS1, with the circle color indicating the residual hydrogen envelope mass (see color bar). The red star shows the terminal stage of the model for M31-2014-DS1, while the gray plus symbol shows the same for our modeling of NGC 6946-BH1. Error bars are shown at 1σ confidence.

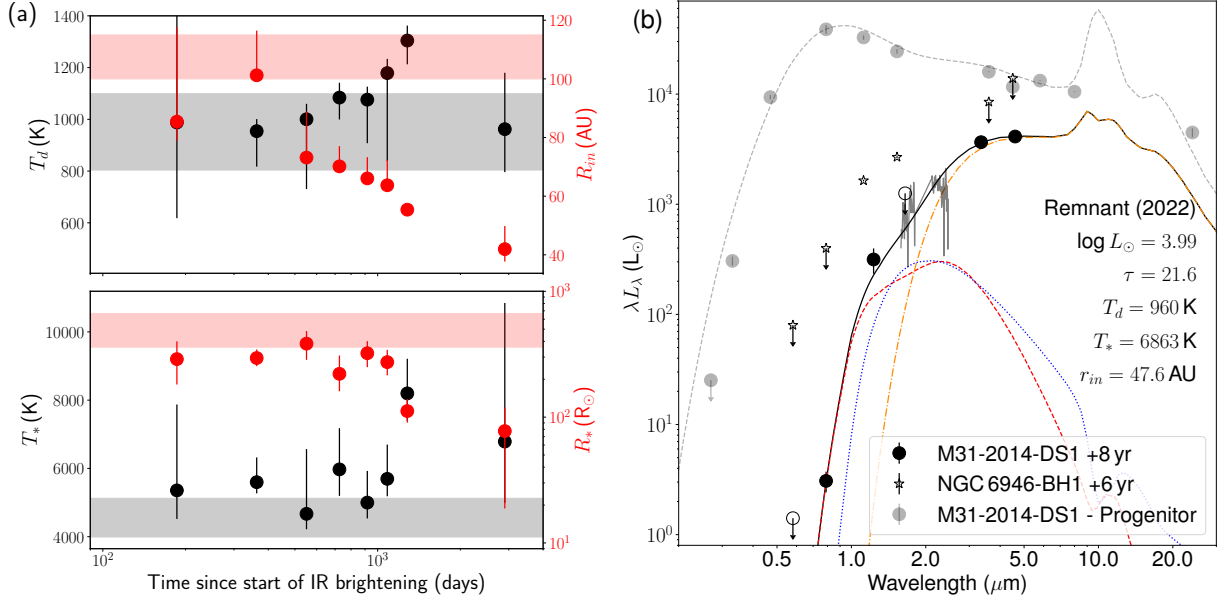


Figure 3: The evolution of the stellar and dust properties, leading to the current remnant of M31-2014-DS1. (a) The temporal evolution of the dust temperature and inner shell radius (top panel), and the inferred stellar radius and photospheric temperature (lower panel). The x-axis indicates time since the start of the IR brightening in 2014 (Figure 1). The shaded regions show the corresponding progenitor parameters. (b) The SED of the remnant of M31-2014-DS1 in 2022 – 2023 (photometry in black circles and spectrum in gray lines). The best-fit DUSTY model is shown (along with parameters) as in Figure 2. The corresponding progenitor photometry and SED model are shown as gray circles and dashed lines, respectively. The SED of NGC 6946-BH1 at a similar phase is shown. Error bars are shown at 1σ confidence, and 5σ upper limits are shown as symbols with downward arrows.

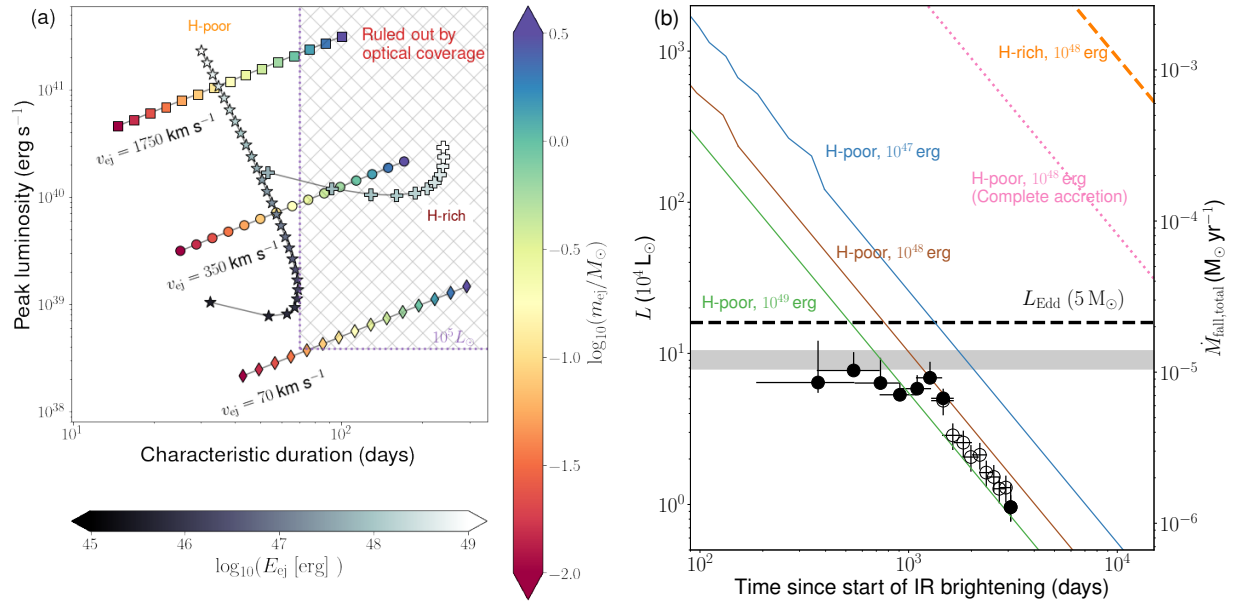


Figure 4: Constraints on mass ejection and fallback of the stellar envelope in M31-2014-DS1.

(a) The expected luminosity and duration of transients powered by hydrogen recombination for ejecta at different velocities and explosion energies. The diamonds, circles and squares correspond to ejecta with fixed velocities of $\approx 1\times$, $\approx 5\times$ and $\approx 25\times$ the estimated escape velocity of the progenitor star, while their colors indicate a sequence of ejecta masses (shown in the right colorbar). The hatched area indicates the phase space of outbursts ruled out by the optical coverage (Materials and Methods). We also show the model luminosity and transient duration expected for our H-poor (stars) and H-rich (plus symbols) progenitor models as a function of the injected explosion energy (shown in the bottom colorbar; Materials and Methods).

(b) The bolometric fading of M31-2014-DS1 compared to models of the mass infall rate from fall-back accretion for different explosion energies (indicated in the figure with different colors) with the nominal H-poor (solid lines) progenitor model and accretion radiative efficiency $\eta = 0.05$. For comparison, we also show the expected fall-back evolution with one fixed explosion energy for the case of complete accretion in the H-poor model (dotted line) and for the H-rich model (dashed line; Materials and Methods). Black solid circles indicate measurements derived from optical to MIR SED modeling and hollow circles indicate estimates derived from applying a bolometric correction to the MIR luminosity. Error bars are shown at 1σ confidence. The gray shaded region shows the estimated progenitor luminosity, while the black dashed line shows the Eddington luminosity for a $5 M_{\odot}$ BH. The right y-axis shows the corresponding total mass fall-back rate into the core.

References and Notes

1. H. T. Janka, K. Langanke, A. Marek, G. Martínez-Pinedo, B. Müller, Theory of core-collapse supernovae. *Phys. Rep.* **442** (1-6), 38–74 (2007), doi:10.1016/j.physrep.2007.02.002.
2. A. Burrows, D. Vartanyan, Core-collapse supernova explosion theory. *Nature* **589** (7840), 29–39 (2021), doi:10.1038/s41586-020-03059-w.
3. N. Langer, Presupernova Evolution of Massive Single and Binary Stars. *Ann. Rev. Astron. Astrophys.* **50**, 107–164 (2012), doi:10.1146/annurev-astro-081811-125534.
4. S. J. Smartt, Progenitors of Core-Collapse Supernovae. *Ann. Rev. Astron. Astrophys.* **47** (1), 63–106 (2009), doi:10.1146/annurev-astro-082708-101737.
5. E. O’Connor, C. D. Ott, Black Hole Formation in Failing Core-Collapse Supernovae. *Astrophys. J.* **730** (2), 70 (2011), doi:10.1088/0004-637X/730/2/70.
6. C. S. Kochanek, *et al.*, A Survey About Nothing: Monitoring a Million Supergiants for Failed Supernovae. *Astrophys. J.* **684** (2), 1336–1342 (2008), doi:10.1086/590053.
7. M. Ivanov, R. Fernández, Mass Ejection in Failed Supernovae: Equation of State and Neutrino Loss Dependence. *Astrophys. J.* **911** (1), 6 (2021), doi:10.3847/1538-4357/abe59e.
8. A. Gilkis, N. Soker, Triggering jet-driven explosions of core-collapse supernovae by accretion from convective regions. *Mon. Not. R. Astron. Soc.* **439** (4), 4011–4017 (2014), doi:10.1093/mnras/stu257.
9. A. Gilkis, N. Soker, Angular Momentum Fluctuations in the Convective Helium Shell of Massive Stars. *Astrophys. J.* **827** (1), 40 (2016), doi:10.3847/0004-637X/827/1/40.
10. E. Quataert, D. Lecoanet, E. R. Coughlin, Black hole accretion discs and luminous transients in failed supernovae from non-rotating supergiants. *Mon. Not. R. Astron. Soc.* **485** (1), L83–L88 (2019), doi:10.1093/mnrasl/slz031.
11. A. Antoni, E. Quataert, Numerical simulations of the random angular momentum in convection: Implications for supergiant collapse to form black holes. *Mon. Not. R. Astron. Soc.* **511** (1), 176–197 (2022), doi:10.1093/mnras/stab3776.

12. A. Antoni, E. Quataert, Numerical simulations of the random angular momentum in convection - II. Delayed explosions of red supergiants following 'failed' supernovae. *Mon. Not. R. Astron. Soc.* **525** (1), 1229–1245 (2023), doi:10.1093/mnras/stad2328.
13. E. Lovegrove, S. E. Woosley, Very Low Energy Supernovae from Neutrino Mass Loss. *Astrophys. J.* **769** (2), 109 (2013), doi:10.1088/0004-637X/769/2/109.
14. E. R. Coughlin, E. Quataert, R. Fernández, D. Kasen, A physical model of mass ejection in failed supernovae. *Mon. Not. R. Astron. Soc.* **477** (1), 1225–1238 (2018), doi:10.1093/mnras/sty667.
15. R. Fernández, E. Quataert, K. Kashiyama, E. R. Coughlin, Mass ejection in failed supernovae: variation with stellar progenitor. *Mon. Not. R. Astron. Soc.* **476** (2), 2366–2383 (2018), doi:10.1093/mnras/sty306.
16. C. S. Kochanek, The Astrophysical Implications of Dust Formation during the Eruptions of Hot, Massive Stars. *Astrophys. J.* **743** (1), 73 (2011), doi:10.1088/0004-637X/743/1/73.
17. K. De, *et al.*, An infrared transient from a star engulfing a planet. *Nature* **617** (7959), 55–60 (2023), doi:10.1038/s41586-023-05842-x.
18. A. Mainzer, *et al.*, Initial Performance of the NEOWISE Reactivation Mission. *Astrophys. J.* **792** (1), 30 (2014), doi:10.1088/0004-637X/792/1/30.
19. E. L. Wright, *et al.*, The Wide-field Infrared Survey Explorer (WISE): Mission Description and Initial On-orbit Performance. *Astron. J.* **140** (6), 1868–1881 (2010), doi:10.1088/0004-6256/140/6/1868.
20. J. Kaluzny, *et al.*, DIRECT Distances to Nearby Galaxies Using Detached Eclipsing Binaries and Cepheids. I. Variables in the Field M31B. *Astron. J.* **115** (3), 1016–1044 (1998), doi:10.1086/300235.
21. P. Massey, K. F. Neugent, E. M. Levesque, M. R. Drout, S. Courteau, The Red Supergiant Content of M31 and M33. *Astron. J.* **161** (2), 79 (2021), doi:10.3847/1538-3881/abd01f.

22. J. Choi, *et al.*, Mesa Isochrones and Stellar Tracks (MIST). I. Solar-scaled Models. *Astrophys. J.* **823** (2), 102 (2016), doi:10.3847/0004-637X/823/2/102.
23. C. Georgy, Yellow supergiants as supernova progenitors: an indication of strong mass loss for red supergiants? *Astron. & Astrophys.* **538**, L8 (2012), doi:10.1051/0004-6361/201118372.
24. S.-C. Yoon, M. Cantiello, Evolution of Massive Stars with Pulsation-driven Superwinds During the Red Supergiant Phase. *Astrophys. J.* **717** (1), L62–L65 (2010), doi:10.1088/2041-8205/717/1/L62.
25. B. Paxton, *et al.*, Modules for Experiments in Stellar Astrophysics (MESA). *Astrophys. J. Suppl.* **192** (1), 3 (2011), doi:10.1088/0067-0049/192/1/3.
26. D. W. Evans, *et al.*, Gaia Data Release 3. The Gaia Andromeda Photometric Survey. *Astron. & Astrophys.* **674**, A4 (2023), doi:10.1051/0004-6361/202244204.
27. L. L. Kiss, G. M. Szabó, T. R. Bedding, Variability in red supergiant stars: pulsations, long secondary periods and convection noise. *Mon. Not. R. Astron. Soc.* **372** (4), 1721–1734 (2006), doi:10.1111/j.1365-2966.2006.10973.x.
28. C. Conroy, *et al.*, A Complete Census of Luminous Stellar Variability on Day to Decade Timescales. *Astrophys. J.* **864** (2), 111 (2018), doi:10.3847/1538-4357/aad460.
29. P. Podsiadlowski, On the Evolution and Appearance of a Surviving Companion after a Type Ia Supernova Explosion. *arXiv e-prints* astro-ph/0303660 (2003), doi:10.48550/arXiv.astro-ph/0303660.
30. B. Mukhija, A. Kashi, Giant Eruptions in Massive Stars and their Effect on the Stellar Structure. *arXiv e-prints* arXiv:2408.01718 (2024), doi:10.48550/arXiv.2408.01718.
31. M. S. Hjellming, R. F. Webbink, Thresholds for Rapid Mass Transfer in Binary System. I. Polytropic Models. *Astrophys. J.* **318**, 794 (1987), doi:10.1086/165412.
32. J. E. Jencson, *et al.*, An Exceptional Dimming Event for a Massive, Cool Supergiant in M51. *Astrophys. J.* **930** (1), 81 (2022), doi:10.3847/1538-4357/ac626c.

33. A. K. Dupree, *et al.*, The Great Dimming of Betelgeuse: A Surface Mass Ejection and Its Consequences. *Astrophys. J.* **936** (1), 18 (2022), doi:10.3847/1538-4357/ac7853.
34. D. Kasen, S. E. Woosley, Type II Supernovae: Model Light Curves and Standard Candle Relationships. *Astrophys. J.* **703** (2), 2205–2216 (2009), doi:10.1088/0004-637X/703/2/2205.
35. T. Matsumoto, B. D. Metzger, Light Curve Model for Luminous Red Novae and Inferences about the Ejecta of Stellar Mergers. *arXiv e-prints* arXiv:2202.10478 (2022).
36. V. Kalogera, G. Baym, The Maximum Mass of a Neutron Star. *Astrophys. J.* **470**, L61 (1996), doi:10.1086/310296.
37. E. Quataert, D. Kasen, Swift 1644+57: the longest gamma-ray burst? *Mon. Not. R. Astron. Soc.* **419** (1), L1–L5 (2012), doi:10.1111/j.1745-3933.2011.01151.x10.1086/141928.
38. A. S. Schneider, E. O'Connor, A Parameterized Neutrino Emission Model to Study Mass Ejection in Failed Core-collapse Supernovae. *arXiv e-prints* arXiv:2209.15064 (2022), doi:10.48550/arXiv.2209.15064.
39. J. M. Blondin, Hypercritical Spherical Accretion onto Compact Objects. *Astrophys. J.* **308**, 755 (1986), doi:10.1086/164548.
40. W. Xu, Simple Convective Accretion Flows (SCAFs): Explaining the ≈ -1 Density Scaling of Hot Accretion Flows around Compact Accreitors. *Astrophys. J.* **954** (2), 180 (2023), doi:10.3847/1538-4357/ace892.
41. J. R. Gerke, C. S. Kochanek, K. Z. Stanek, The search for failed supernovae with the Large Binocular Telescope: first candidates. *Mon. Not. R. Astron. Soc.* **450** (3), 3289–3305 (2015), doi:10.1093/mnras/stv776.
42. S. M. Adams, C. S. Kochanek, J. R. Gerke, K. Z. Stanek, X. Dai, The search for failed supernovae with the Large Binocular Telescope: confirmation of a disappearing star. *Mon. Not. R. Astron. Soc.* **468** (4), 4968–4981 (2017), doi:10.1093/mnras/stx816.

43. C. M. Basinger, C. S. Kochanek, S. M. Adams, X. Dai, K. Z. Stanek, The search for failed supernovae with the Large Binocular Telescope: N6946-BH1, still no star. *Mon. Not. R. Astron. Soc.* **508** (1), 1156–1164 (2021), doi:10.1093/mnras/stab2620.
44. A. Kashi, N. Soker, Type II intermediate-luminosity optical transients (ILOTs). *Mon. Not. R. Astron. Soc.* **467** (3), 3299–3305 (2017), doi:10.1093/mnras/stx240.
45. E. R. Beasor, *et al.*, JWST reveals a luminous infrared source at the position of the failed supernova candidate N6946-BH1. *arXiv e-prints* arXiv:2309.16121 (2023), doi:10.48550/arXiv.2309.16121.
46. R. M. Humphreys, Comments on the Progenitor of NGC 6946-BH1. *Research Notes of the American Astronomical Society* **3** (10), 164 (2019), doi:10.3847/2515-5172/ab5191.
47. C. S. Kochanek, J. M. M. Neustadt, K. Z. Stanek, The search for failed supernovae with the Large BinocularTelescope: The Mid-IR Counterpart to N6946-BH1. *arXiv e-prints* arXiv:2310.01514 (2023), doi:10.48550/arXiv.2310.01514.
48. G. de Vaucouleurs, J. Corwin, H. G., S Andromedae 1885: A Centennial Review. *Astrophys. J.* **295**, 287 (1985), doi:10.1086/163374.
49. S. Balberg, L. Zampieri, S. L. Shapiro, Black Hole Emergence in Supernovae. *Astrophys. J.* **541** (2), 860–882 (2000), doi:10.1086/309472.
50. D. Vartanyan, A. Burrows, T. Wang, M. S. B. Coleman, C. J. White, Gravitational-wave signature of core-collapse supernovae. *Phys. Rev. D* **107** (10), 103015 (2023), doi:10.1103/PhysRevD.107.103015.
51. C. Lunardini, Diffuse Neutrino Flux from Failed Supernovae. *Phys. Rev. Lett.* **102** (23), 231101 (2009), doi:10.1103/PhysRevLett.102.231101.
52. T. Sukhbold, S. Adams, Missing red supergiants and carbon burning. *Mon. Not. R. Astron. Soc.* **492** (2), 2578–2587 (2020), doi:10.1093/mnras/staa059.
53. L. Boccioli, L. Roberti, The Physics of Core-Collapse Supernovae: Explosion Mechanism and Explosive Nucleosynthesis. *Universe* **10** (3), 148 (2024), doi:10.3390/universe10030148.

54. T. Sukbold, T. Ertl, S. E. Woosley, J. M. Brown, H. T. Janka, Core-collapse Supernovae from 9 to 120 Solar Masses Based on Neutrino-powered Explosions. *Astrophys. J.* **821** (1), 38 (2016), doi:10.3847/0004-637X/821/1/38.
55. K. C. Chambers, *et al.*, The Pan-STARRS1 Surveys. *arXiv e-prints* arXiv:1612.05560 (2016).
56. A. Rau, *et al.*, Exploring the Optical Transient Sky with the Palomar Transient Factory. *PASP* **121** (886), 1334 (2009), doi:10.1086/605911.
57. M. J. Graham, *et al.*, The Zwicky Transient Facility: Science Objectives. *PASP* **131** (7), 078001 (2019), doi:10.1088/1538-3873/ab006c.
58. S. J. Smartt, Observational Constraints on the Progenitors of Core-Collapse Supernovae: The Case for Missing High-Mass Stars. *PASA* **32**, e016 (2015), doi:10.1017/pasa.2015.17.
59. D. Lang, unWISE: Unblurred Coadds of the WISE Imaging. *Astron. J.* **147** (5), 108 (2014), doi:10.1088/0004-6256/147/5/108.
60. A. M. Meisner, D. Lang, D. J. Schlegel, Time-resolved WISE/NEOWISE Coadds. *Astron. J.* **156** (2), 69 (2018), doi:10.3847/1538-3881/aacbcd.
61. K. De, *et al.*, Palomar Gattini-IR: Survey Overview, Data Processing System, On-sky Performance and First Results. *PASP* **132** (1008), 025001 (2020), doi:10.1088/1538-3873/ab6069.
62. B. Zackay, E. O. Ofek, A. Gal-Yam, Proper Image Subtraction - Optimal Transient Detection, Photometry, and Hypothesis Testing. *Astrophys. J.* **830**, 27 (2016), doi:10.3847/0004-637X/830/1/27.
63. S. van der Walt, A. Crellin-Quick, J. Bloom, SkyPortal: An Astronomical Data Platform. *The Journal of Open Source Software* **4** (37), 1247 (2019), doi:10.21105/joss.01247.
64. Gaia Collaboration, *et al.*, Gaia Early Data Release 3. Summary of the contents and survey properties. *Astron. & Astrophys.* **649**, A1 (2021), doi:10.1051/0004-6361/202039657.
65. D. G. Monet, *et al.*, The USNO-B Catalog. *Astron. J.* **125** (2), 984–993 (2003), doi:10.1086/345888.

66. M. F. Skrutskie, *et al.*, The Two Micron All Sky Survey (2MASS). *Astron. J.* **131** (2), 1163–1183 (2006), doi:10.1086/498708.
67. N. M. Law, *et al.*, The Palomar Transient Factory: System Overview, Performance, and First Results. *PASP* **121** (886), 1395 (2009), doi:10.1086/648598.
68. E. O. Ofek, *et al.*, The Palomar Transient Factory photometric catalog 1.0. *PASP* **124** (918), 854 (2012), doi:10.1086/666978.
69. H. A. Flewelling, *et al.*, The Pan-STARRS1 Database and Data Products. *Astrophys. J. Suppl.* **251** (1), 7 (2020), doi:10.3847/1538-4365/abb82d.
70. E. C. Bellm, *et al.*, The Zwicky Transient Facility: System Overview, Performance, and First Results. *PASP* **131** (1), 018002 (2019), doi:10.1088/1538-3873/aaecbe.
71. F. J. Masci, *et al.*, The Zwicky Transient Facility: Data Processing, Products, and Archive. *PASP* **131** (1), 018003 (2019), doi:10.1088/1538-3873/aae8ac.
72. J. J. Dalcanton, *et al.*, The Panchromatic Hubble Andromeda Treasury. *Astrophys. J. Suppl.* **200** (2), 18 (2012), doi:10.1088/0067-0049/200/2/18.
73. A. E. Dolphin, WFPC2 Stellar Photometry with HSTPHOT. *PASP* **112**, 1383–1396 (2000), doi:10.1086/316630.
74. A. Dolphin, DOLPHOT: Stellar photometry, *Astrophysics Source Code Library* (2016).
75. B. F. Williams, *et al.*, The Panchromatic Hubble Andromeda Treasury. X. Ultraviolet to Infrared Photometry of 117 Million Equidistant Stars. *Astrophys. J. Suppl.* **215** (1), 9 (2014), doi:10.1088/0067-0049/215/1/9.
76. R. C. Bohlin, Perfecting the Photometric Calibration of the ACS CCD Cameras. *Astron. J.* **152** (3), 60 (2016), doi:10.3847/0004-6256/152/3/60.
77. Spitzer Science Center (SSC), Infrared Science Archive (IRSA), VizieR Online Data Catalog: The Spitzer (SEIP) source list (SSTSL2) (Spitzer Science Center, 2021). *VizieR Online Data Catalog II/368* (2021).

78. G. G. Fazio, *et al.*, The Infrared Array Camera (IRAC) for the Spitzer Space Telescope. *Astrophys. J. Suppl.* **154** (1), 10–17 (2004), doi:10.1086/422843.
79. G. H. Rieke, *et al.*, The Multiband Imaging Photometer for Spitzer (MIPS). *Astrophys. J. Suppl.* **154** (1), 25–29 (2004), doi:10.1086/422717.
80. D. Fabricant, *et al.*, Binospec: A Wide-field Imaging Spectrograph for the MMT. *PASP* **131** (1001), 075004 (2019), doi:10.1088/1538-3873/ab1d78.
81. K. De, *et al.*, The Zwicky Transient Facility Census of the Local Universe. I. Systematic Search for Calcium-rich Gap Transients Reveals Three Related Spectroscopic Subclasses. *Astrophys. J.* **905** (1), 58 (2020), doi:10.3847/1538-4357/abb45c.
82. J. T. Rayner, *et al.*, SpeX: A Medium-Resolution 0.8-5.5 Micron Spectrograph and Imager for the NASA Infrared Telescope Facility. *PASP* **115** (805), 362–382 (2003), doi:10.1086/367745.
83. I. S. McLean, *et al.*, MOSFIRE, the multi-object spectrometer for infra-red exploration at the Keck Observatory, in *Ground-based and Airborne Instrumentation for Astronomy IV*, I. S. McLean, S. K. Ramsay, H. Takami, Eds., vol. 8446 of *Society of Photo-Optical Instrumentation Engineers (SPIE) Conference Series* (2012), p. 84460J, doi:10.1117/12.924794.
84. J. C. Wilson, *et al.*, Mass producing an efficient NIR spectrograph, in *Ground-based Instrumentation for Astronomy*, A. F. M. Moorwood, M. Iye, Eds., vol. 5492 of *Society of Photo-Optical Instrumentation Engineers (SPIE) Conference Series* (2004), pp. 1295–1305, doi:10.1117/12.550925.
85. M. C. Cushing, W. D. Vacca, J. T. Rayner, Spextool: A Spectral Extraction Package for SpeX, a 0.8-5.5 Micron Cross-Dispersed Spectrograph. *PASP* **116**, 362–376 (2004), doi:10.1086/382907.
86. W. D. Vacca, M. C. Cushing, J. T. Rayner, A Method of Correcting Near-Infrared Spectra for Telluric Absorption. *PASP* **115**, 389–409 (2003), doi:10.1086/346193.
87. A. Fruscione, *et al.*, CIAO: Chandra’s data analysis system, in *Society of Photo-Optical Instrumentation Engineers (SPIE) Conference Series*, D. R. Silva, R. E. Doxsey, Eds., vol.

- 6270 of *Society of Photo-Optical Instrumentation Engineers (SPIE) Conference Series* (2006), p. 62701V, doi:10.1117/12.671760.
88. HI4PI Collaboration, *et al.*, HI4PI: A full-sky H I survey based on EBHIS and GASS. *Astron. & Astrophys.* **594**, A116 (2016), doi:10.1051/0004-6361/201629178.
 89. P. A. Evans, *et al.*, An online repository of Swift/XRT light curves of γ -ray bursts. *Astron. & Astrophys.* **469** (1), 379–385 (2007), doi:10.1051/0004-6361:20077530.
 90. P. A. Evans, *et al.*, Methods and results of an automatic analysis of a complete sample of Swift-XRT observations of GRBs. *Mon. Not. R. Astron. Soc.* **397** (3), 1177–1201 (2009), doi:10.1111/j.1365-2966.2009.14913.x.
 91. Z. Ivezić, M. Elitzur, Self-similarity and scaling behaviour of infrared emission from radiatively heated dust - I. Theory. *Mon. Not. R. Astron. Soc.* **287** (4), 799–811 (1997), doi:10.1093/mnras/287.4.799.
 92. Z. Ivezić, M. Nenkova, M. Elitzur, User Manual for DUSTY. *arXiv e-prints* astro-ph/9910475 (1999).
 93. T. Verhoelst, *et al.*, The dust condensation sequence in red supergiant stars. *Astron. & Astrophys.* **498** (1), 127–138 (2009), doi:10.1051/0004-6361/20079063.
 94. J. S. Mathis, W. Rumpl, K. H. Nordsieck, The size distribution of interstellar grains. *Astrophys. J.* **217**, 425–433 (1977), doi:10.1086/155591.
 95. K. De, *et al.*, SRGA J181414.6-225604: A new Galactic symbiotic X-ray binary outburst triggered by an intense mass loss episode of a heavily obscured Mira variable. *arXiv e-prints* arXiv:2205.09139 (2022).
 96. D. Foreman-Mackey, D. W. Hogg, D. Lang, J. Goodman, emcee: The MCMC Hammer. *PASP* **125** (925), 306 (2013), doi:10.1086/670067.
 97. E. L. Fitzpatrick, Correcting for the Effects of Interstellar Extinction. *PASP* **111** (755), 63–75 (1999), doi:10.1086/316293.

98. E. F. Schlafly, D. P. Finkbeiner, Measuring Reddening with Sloan Digital Sky Survey Stellar Spectra and Recalibrating SFD. *Astrophys. J.* **737** (2), 103 (2011), doi:10.1088/0004-637X/737/2/103.
99. B. T. Draine, A. Li, Infrared Emission from Interstellar Dust. IV. The Silicate-Graphite-PAH Model in the Post-Spitzer Era. *Astrophys. J.* **657** (2), 810–837 (2007), doi:10.1086/511055.
100. L. Dessart, E. Livne, R. Waldman, Shock-heating of stellar envelopes: a possible common mechanism at the origin of explosions and eruptions in massive stars. *Mon. Not. R. Astron. Soc.* **405** (4), 2113–2131 (2010), doi:10.1111/j.1365-2966.2010.16626.x.
101. J. A. Goldberg, L. Bildsten, B. Paxton, Inferring Explosion Properties from Type II-Plateau Supernova Light Curves. *Astrophys. J.* **879** (1), 3 (2019), doi:10.3847/1538-4357/ab22b6.
102. I. K. W. Kleiser, D. Kasen, Rapidly fading supernovae from massive star explosions. *Mon. Not. R. Astron. Soc.* **438** (1), 318–328 (2014), doi:10.1093/mnras/stt2191.
103. E. R. Coughlin, E. Quataert, S. Ro, Weak Shock Propagation with Accretion. I. Self-similar Solutions and Application to Failed Supernovae. *Astrophys. J.* **863** (2), 158 (2018), doi:10.3847/1538-4357/aad198.

Acknowledgments

We thank H. Gupta, K. Das and P. Nair for assistance with the observations. We thank S. R. Kulkarni, L. Hillenbrand, J. Goldberg and C. Conroy for valuable discussions. Data presented herein were obtained at the W. M. Keck Observatory from telescope time allocated to the National Aeronautics and Space Administration through the agency's scientific partnership with the California Institute of Technology and the University of California. The Observatory was made possible by the generous financial support of the W. M. Keck Foundation. The authors wish to recognize and acknowledge the very significant cultural role and reverence that the summit of Maunakea has always had within the indigenous Hawaiian community. We are most fortunate to have the opportunity to conduct observations from this mountain. This research has made use of the Keck Observatory Archive (KOA), which is operated by the W. M. Keck Observatory and the NASA Exoplanet Science

Institute (NExSci), under contract with the National Aeronautics and Space Administration. We acknowledge the Visiting Astronomer Facility at the Infrared Telescope Facility, which is operated by the University of Hawaii under contract 80HQTR19D0030 with the National Aeronautics and Space Administration.

Funding: K. D.’s work was supported by NASA through the NASA Hubble Fellowship grant #HST-HF2-51477.001 awarded by the Space Telescope Science Institute, which is operated by the Association of Universities for Research in Astronomy, Inc., for NASA, under contract NAS5-26555. M.MacLeod is grateful for support from a Clay postdoctoral fellowship at the Smithsonian Astrophysical Observatory. A.A. is grateful for support from the Simons Foundation through a Flatiron Research Fellowship. This research benefited from interactions at workshops funded by the Gordon and Betty Moore Foundation through grant GBMF5076. This work was supported by a NASA Keck PI Data Award, administered by the NASA Exoplanet Science Institute.

Author contributions: K.D. identified the object, initiated follow-up observations, carried out the analysis and wrote the manuscript. M.MacLeod developed theoretical models and helped write the manuscript. J.E.J. carried out archival space based analysis and R.M.L. assisted with observational interpretation. A.A., A.L., E.L. and E.Q. helped with theoretical interpretation. M.M.K. and R.S. assisted with ground-based observational follow-up. E.K., M.Masterson and C.P. carried out X-ray data analysis. A.M.M. assisted with use of WISE images. All authors contributed to the scientific interpretation.

Competing interests: There are no competing interests to declare.

Data and materials availability: All the data used in this work are provided in the Supplementary Material. The first author will provide python code used to analyze the observations, and any data used to generate figures, upon request. The theoretical MESA models and their interpretation as failed supernovae is available at <https://github.com/morganemacleod/FailedSNCalcs>.

Supplementary materials

Materials and Methods

Supplementary Text

Figs. S1 to S9

Tables S1 to S2

References (59-103)

Supplementary Materials for

The disappearance of a massive star marking the birth of a

black hole in M31

Kishalay De^{1*}, Morgan MacLeod², Jacob E. Jencson³, Elizabeth Lovegrove⁴,
Andrea Antoni⁵, Erin Kara¹, Mansi M. Kasliwal⁶, Ryan M. Lau⁷, Abraham Loeb^{2,8},
Megan Masterson¹, Aaron M. Meisner⁷, Christos Panagiotou¹, Eliot Quataert⁹
and Robert Simcoe¹

¹ Kavli Institute for Astrophysics and Space Research, Massachusetts Institute of Technology, Cambridge,
MA 02139, USA

² Center for Astrophysics — Harvard & Smithsonian 60 Garden Street, MS-16, Cambridge, MA 02138,
USA

³ Department of Physics and Astronomy, Johns Hopkins University, Baltimore, MD 21218, USA

⁴ United States Naval Observatory

⁵ Center for Computational Astrophysics, Flatiron Institute, New York, NY 10010, USA

⁶ Cahill Center for Astrophysics, California Institute of Technology, 1200 E. California Boulevard,
Pasadena,
CA 91125, USA

⁷ NSF's National Optical-Infrared Astronomy Research Laboratory, 950 N. Cherry Ave., Tucson,
AZ 85719, USA

⁸ Black Hole Initiative, Harvard University, Cambridge, MA 02138, USA

⁹ Department of Astrophysical Sciences, Princeton University, Princeton, NJ 08544, USA

*Corresponding author. Email: kde1@mit.edu

This PDF file includes:

Materials and Methods

Supplementary Text

Figs. S1 to S9

Tables S1 to S2

References (60-103)

Materials and Methods

Discovery in NEOWISE

The Wide-field Infrared Survey Explorer (WISE) satellite (19), re-initiated as the NEOWISE mission (18), has been carrying out an all-sky MIR survey in the W1 ($3.4\text{ }\mu\text{m}$) and W2 ($4.6\text{ }\mu\text{m}$) bands since 2014. In its ongoing survey, NEOWISE revisits each part of the sky once every ≈ 0.5 yr. We have carried out a systematic search for transients in time-resolved coadded images created as part of the unWISE project (59, 60), the details of which will be presented in De et al. (in prep). In brief, we used a customized code (61) based on the ZOGY algorithm (62) to perform image subtraction on the NEOWISE images using the co-added images of the WISE mission (obtained in 2010-2011) as reference images. The pipeline produces a database of all transients down to a statistical significance of $\approx 10\sigma$. Follow-up for the sources was coordinated using the `fritz` astronomical data platform (63).

As part of an ongoing program to identify candidate novae and stellar mergers in M31 over the last decade, we applied custom selection criteria to the catalog of WISE transients and selected luminous MIR outbursts spatially coincident with M31 satisfying the following criteria:

1. The transient should be located within 4 degrees of the nucleus of M31.
2. The source should have brightened from the reference image and have no prior history of outbursts or variability in WISE data before the flagged brightening. The transient should be detected in at least two consecutive epochs to reject foreground moving objects.
3. The transient should not be coincident with a foreground Galactic star, as confirmed from parallax and proper motion measurements from the Gaia mission (64).
4. The transient should reach a peak MIR luminosity of $\gtrsim 10^{37}\text{ erg s}^{-1}$ to select outbursts that reach the expected Eddington luminosity for a $\approx 0.1 - 1\text{ M}_\odot$ star, as well as reject lower luminosity IR outbursts from young stars and X-ray binaries.

We identified the source WTP 16aathy as a candidate nova at a projected separation of $\approx 0.54^\circ$ ($\approx 7\text{ kpc}$) from the nucleus of M31. The transient was first detected at $> 10\sigma$ significance in difference imaging for the NEOWISE observation of the field in 2016 July (MJD 57591.79) at a

(host subtracted) magnitude of $W2 = 17.91 \pm 0.10$ AB mag. The transient is coincident with an optical point source clearly detected in archival ground-based imaging and reported in Gaia DR3 at J2000 coordinates $\alpha = 00:45:13.47$, $\delta = +41:32:33.14$. Given the lower spatial resolution of WISE, we use the Gaia coordinates of the optical source for the rest of this work. The optical source has no significant parallax ($\pi = 0.09 \pm 0.23$ mas) or proper motion ($\mu_{RA} = -0.17 \pm 0.17$, $\mu_{Dec} = -0.10 \pm 0.21$) detected in Gaia DR3, arguing against its classification as a foreground Galactic star. Performing forced photometry at the Gaia position on the difference images, we find the IR brightening of the source to have begun in the first NEOWISE visit of the field on MJD 56674.19. We nominally adopt this time as the reference time for our analysis, and use the name M31-2014-DS1 denoting the onset year of the event. Although the exact time of the start of the IR brightening is not well constrained, our derived quantitative estimates are corroborated by the magnitude of the bolometric fading (by $\approx 10\times$) over ≈ 1000 d after the MIR peak.

Archival photometry

The progenitor of M31-2014-DS1 has been reported in historical archival optical and infrared source catalogs including USNO-B1.0 (65) and 2MASS (66). It was previously designated as an irregular variable star in the field of M31 (20) and designated the name V7984 M31B. We searched for archival time resolved photometry of the source from ground and space-based surveys. The field was observed with the Palomar Transient Factory (67) between 2010 and 2014 in the r -filter, and we retrieved time resolved photometry of the source from the online catalog (68) at the NASA/IPAC Infrared Science Archive. The source was observed in the $grizy$ filters by the PanSTARRS1 (PS1 (55)) survey between 2010 and 2014, and we retrieved the point source photometry from the online source catalog (69). We derive MIR photometry from NEOWISE images by performing forced PSF photometry on the `unwise` images prior to image subtraction. We retrieved optical photometry of the source between 2014 and 2017 in the Gaia G , BP and RP filters released as part of the Gaia-Andromeda survey (26) in Gaia DR3. While the source was observed as part of the Zwicky Transient Facility (ZTF (70)) optical survey between 2018 and 2024, there is no source detected at the position in g and r -bands, in either the stacked reference image or individual epochs of observation. We derive 5σ upper limits on the source flux by retrieving forced PSF photometry on the ZTF difference images (71), and stacking the non-detection upper limits in bins of 60 d. The

archival light curve is shown in Figure 1, and provided in Table S1.

The source was serendipitously observed using the Hubble Space Telescope (HST) and Spitzer Space Telescope at multiple epochs between 2005 and 2022. We analyzed the available HST imaging from 2012 taken with the Advanced Camera for Surveys (ACS; F475W, F814W) and Wide Field Camera 3 (WFC3) in both the UVIS (F336W, F275W) and IR (F110W, F160W) channels as part of the Panochromatic Hubble Andromeda Treasury (PHAT) program (72) (PID: 12111; PI: J. Dalcanton), as well as the 2016 ACS imaging in F625W (PID: 14072; PI: M. Boyer) and 2022 WFC3/UVIS imaging in F606W and F814W (PID: 16730; PI: N. Lehner). We processed the available *HST* images with DOLPHOT (73, 74) to obtain PSF-fitting photometry of M31-2014-DS1. As inputs to DOLPHOT, we use the CTE-corrected `f1c` frames for ACS/WFC and WFC3/UVIS and `f1t` frames for WFC3/IR downloaded from the Mikulski Archive for Space Telescopes (MAST). We employ the same DOLPHOT parameter settings for each camera as used by PHAT (72, 75). We ran DOLPHOT separately for each instrument and filter combination over the available epochs, using the drizzled 2012 F814W mosaic as a common reference image for alignment across all runs. DOLPHOT computes and applies aperture corrections to a radius of 0.5'' for the reported photometry. We then applied the appropriate corrections to infinite apertures for each instrument and filter combination.¹ We retrieved Spitzer photometry of the source from 2005 as published in the Spitzer source list (77). The photometry was acquired with the Infrared Array Camera (IRAC (78)) in Channels 1 (3.6 μm), 2 (4.5 μm), 3 (5.8 μm) and 4 (8.0 μm), and using the Multiband Imaging Photometer for Spitzer (MIPS (79)) in Channel 1 (24.0 μm). We use the measurements from 2012 and 2022 to characterize the progenitor and remnant of M31-2014-DS1, and list them in Table S2.

Follow-up imaging

We obtained follow-up optical imaging of the source using the Binospec instrument (80) on the MMT telescope, as part of our optical follow-up program for WISE transients (PI: M. MacLeod). Observations were obtained between UT 2023-10-18 and 2023-10-19, consisting of dithered exposures of the field amounting to a total exposure time of 2400 s and 1800 s in the *g* and *r* filters respectively. The data were reduced, stacked and calibrated against the PS1 catalog using a modified

¹See (76) for ACS; for WFC3, see <https://www.stsci.edu/hst/instrumentation/wfc3/data-analysis/photometric-calibration>

version of an optical imaging pipeline (81). We performed aperture photometry at the position of the source, and derive 5σ upper limits of $r > 22.44$ mag and $g > 22.96$ mag, limited primarily by source confusion in the dense field. We obtained near-infrared imaging of the source using the SpeX instrument (82) on the NASA Infrared Telescope Facility on UT 2023-09-06, under program 2023B053 (PI: De). A series of dithered exposures were obtained amounting to a total exposure time of 1200 s in both J and K filters. The images were reduced using a custom infrared image reduction pipeline (81). No source is detected at the transient position to a 5σ limiting magnitude of $J > 19.0$ mag and $K > 17.8$ mag. We obtained deeper near-infrared imaging using the Multi-Object Spectrometer For Infrared Exploration (MOSFIRE (83)) on the Keck-I telescope, on UT 2023-12-25 as part of program 2023B_C358 (PI: Kasliwal). The source was observed over multiple dithered exposures amounting to a total exposure time of 288 s and 297 s in J and K bands respectively, although high wind conditions during the K -band observations preclude a reliable analysis for those images. Performing aperture photometry at the source position, a faint source is detected in the J -band images at $J = 20.90 \pm 0.28$ Vega mag.

Follow-up infrared spectroscopy

On UT 2023-09-04, we obtained follow-up $1.0 - 2.5 \mu\text{m}$ near-infrared spectroscopy of the source using the Near Infrared Echelle Spectrometer (NIRES (84)) on the Keck-II telescope, as part of program 2023B_N258 (PI: De). Due to the faintness of the source, it was acquired by centering a nearby bright star in the slit followed by applying a blind offset using the coordinates reported in Gaia. We obtained a series of dithered exposures in the ABBA pattern amounting to a total exposure time of 2400 s. We reduced the data using the `spextool` (85) software, followed by flux calibration and telluric correction using the `xtellcor` (86) package. A faint source is detected in the spectral trace in H and K bands with a nearly featureless spectrum brightening towards longer wavelengths, shown in Figure 3.

X-ray observations

To constrain the X-ray luminosity of M31-2014-DS1, we retrieved archival observations of the source from the *Chandra* telescope. The source was within the field of view of a 50 ks *Chandra* ACIS-I observation in 2015 (ObsID 17010). We reduced the data using CIAO (87) (version 4.16)

and CALDBv4.11.0, finding that there was no significant detection at the source position. Using the `aplunits` tool and following standard procedures², we estimate a 3σ upper limit on the 0.5-7 keV X-ray flux of $F_X \lesssim 2.0 \times 10^{-15}$ erg s $^{-1}$ cm $^{-2}$ in the 0.5-7 keV band. This limit was calculated using a circular source region with a radius of 5'' and by assuming a $\Gamma = 2$ power-law spectrum with galactic absorption (88) with $N_H = 2.26 \times 10^{21}$ cm $^{-2}$. At a distance of 770 kpc, this corresponds to a luminosity of $L_X \lesssim 1.4 \times 10^{35}$ erg s $^{-1}$. We also searched the *Swift* archive for any observations within 12' of the source after 2015, finding four observations in mid-July 2020 (ObsIDs 00037721002-5). Using the online XRT products generator³ ((89, 90)), we stacked these observations (≈ 4 ks in total) to find a 3σ upper limit on the 0.3-10 keV X-ray flux of $F_X \lesssim 1.3 \times 10^{-13}$ erg s $^{-1}$ cm $^{-2}$ in the 0.3-10 keV band, assuming the same spectral shape as for the *Chandra* observations. Without correcting for any intrinsic absorption, this corresponds to a luminosity limit of $L_X \lesssim 8.9 \times 10^{36}$ erg s $^{-1}$. The source was also observed serendipitously by *NuSTAR* four times in 2015. We followed standard procedure to reduce the observational data using the *nupipeline* and *nuproducts* tools of the *NuSTAR* Data Analysis Software (NuSTARDAS) package version 2.1.2 and the corresponding CALDBv20240422. The source is not detected in any of the observations. Assuming again a photon index of $\Gamma = 2$, we estimated a stacked 3σ upper limit for its 2-10 keV flux of $F_X \lesssim 2.2 \times 10^{-14}$ erg s $^{-1}$ cm $^{-2}$, which corresponds to an observed luminosity of $L_X \lesssim 1.6 \times 10^{36}$ erg s $^{-1}$.

DUSTY modeling

M31-2014-DS1 exhibits bright MIR emission throughout its evolution in the last decade, indicative of dust surrounding the star. Here, we model the optical to MIR SED of the transient to estimate the time evolving properties of the central star and circumstellar dust shell. We use the radiative dust transfer code DUSTY (91, 92) to fit the multi-wavelength data. We assume a spherically symmetric distribution of the dust with a $\propto r^{-2}$ density profile around the star, which is assumed to be a point source. We assume the dust grains to be composed of warm silicates as relevant for massive red supergiants (93), and with a MRN grain size distribution (94) ($\propto a^{-3.5}$) with a minimum and maximum grain size of $a_{min} = 0.005$ μ m and $a_{max} = 0.25$ μ m.

²<https://cxc.cfa.harvard.edu/ciao/threads/upperlimit/index.html>

³https://www.swift.ac.uk/user_objects/

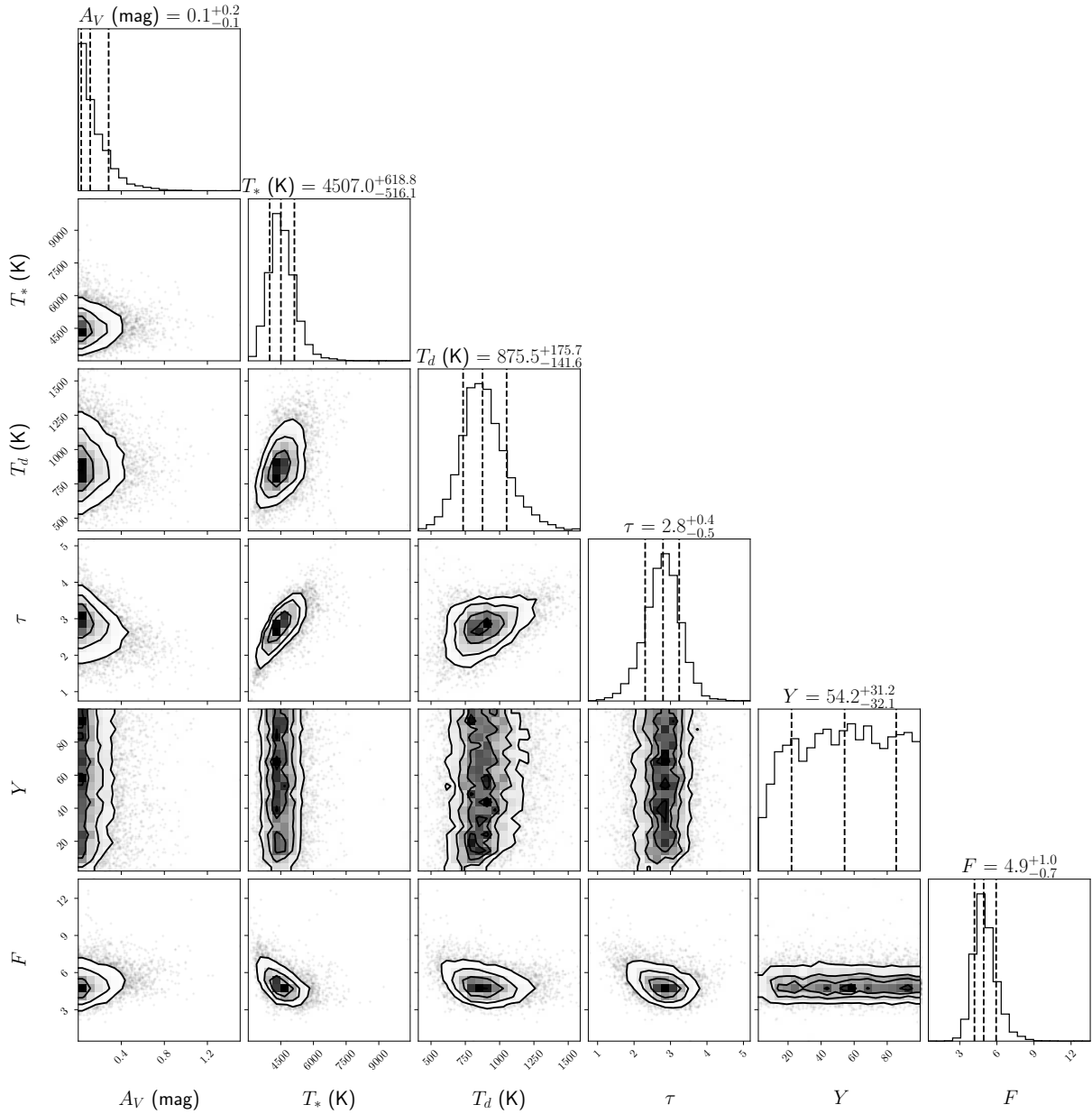


Figure S1: Corner plots showing the model-fit parameters of the MCMC DUSTY modeling of the progenitor of M31-2014-DS1 in 2012. The median of the posterior distributions and the corresponding 68% confidence intervals are indicated in the labels with their corresponding units (the total flux F is reported in $10^{-12} \text{ erg cm}^{-2} \text{ s}^{-1}$), while the same quantities are highlighted with vertical bars in the one dimensional histograms.

Owing to extensive wavelength coverage from ultraviolet to MIR bands, we first fit the progenitor photometry from HST and SST using a Markov Chain Monte Carlo (MCMC) wrapper around the DUSTY code (95) using the Python `emcee` library (96). We model the foreground wavelength

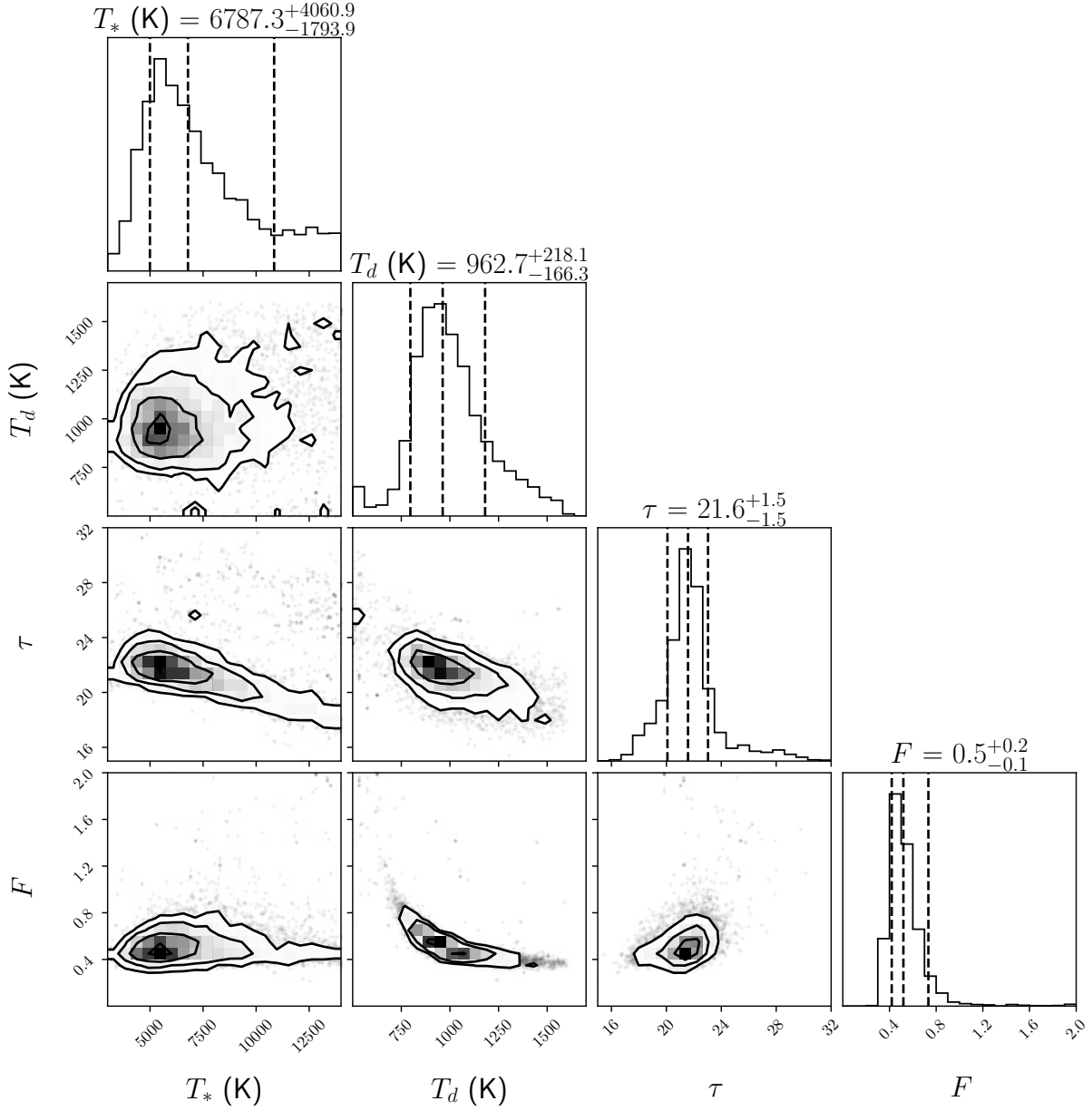


Figure S2: Corner plots showing the model-fit parameters of the MCMC DUSTY modeling of the remnant of M31-2014-DS1 in 2022. The labelling follows the same convention as Figure S1. A_V and Y are not used as free parameters in this fit.

dependent interstellar extinction using a Fitzpatrick law (97) extending from ultraviolet to the MIR. The resulting free parameters of the model are the dust optical depth at 0.55 μm (τ_V), the foreground visual extinction (A_V), the inner stellar temperature (T_*), the dust temperature at the inner edge of the shell (T_d), the thickness of the shell (Y) and the total flux (F). We assume flat priors on all

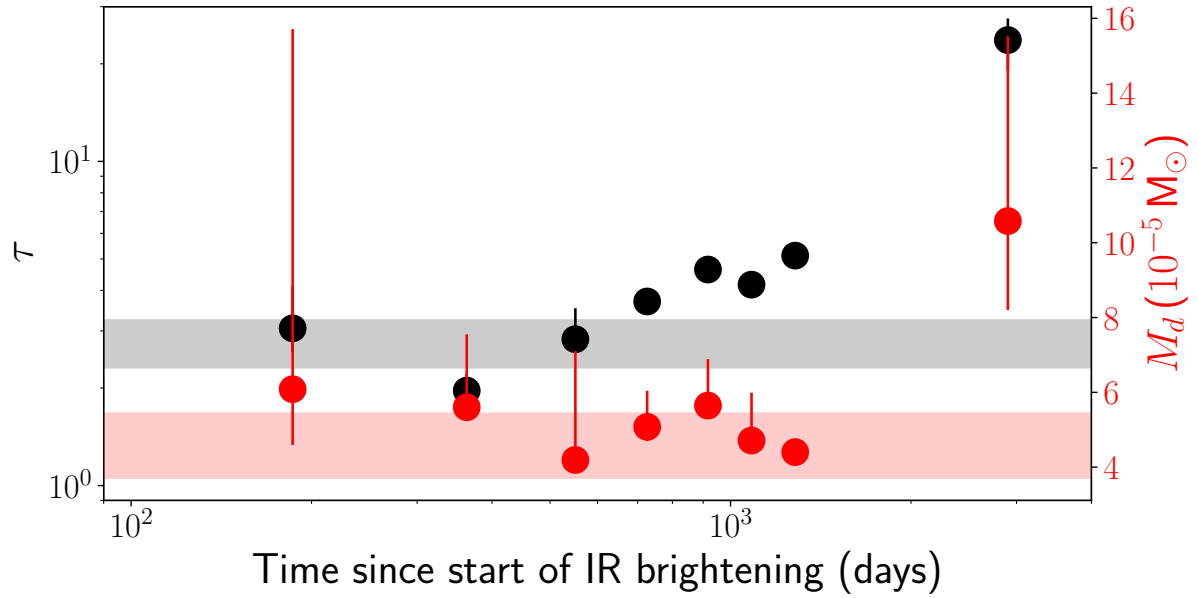


Figure S3: Evolution of the optical depth and total mass of the circumstellar dust shell during the dimming episode. Errors are shown at 1σ confidence level. The gray and red shaded regions show the corresponding parameters for the progenitor SED model.

the fit parameters and ensure convergence of the posterior sampling chains. The resulting posterior distributions are shown in Figure S1.

We find the fitting to be relatively insensitive to the thickness Y because the wavelength coverage is primarily confined to the shorter wavelength MIR bands where the emission is dominated by the hotter, inner part of the dust shell. The best-fit foreground extinction is consistent with the Milky Way extinction ($A_V \approx 0.1$ mag) for this line of sight (98), suggesting no additional host extinction from M31. To constrain the SED of the current remnant, we perform the same analysis using the contemporaneous HST, Keck and NEOWISE data obtained during $\approx 2022 - 2023$, fix the foreground extinction to $A_V = 0.1$ mag and the thickness $Y = 10$ based on the progenitor model. Consistent with the optical disappearance and slow infrared fading, the analysis (Figure S2) reveals a much higher optical depth and $\approx 10\times$ fainter bolometric flux for the current remnant.

To understand the evolution of the source, we use the Gaia multi-color photometric coverage during the optical fading (Figure 1) together with the NEOWISE photometry. Since the Gaia measurements are not strictly simultaneous with the NEOWISE coverage, and because we are interested in the slower long term evolution of the source, we average the Gaia measurements

around the time of the NEOWISE observations (within 1.5 months of each epoch; Figure 1) in creating an optical (Gaia *BP* and *RP*) to MIR (NEOWISE *W1* and *W2*) SED for each NEOWISE epoch. We then perform the same SED fitting for these epochs as in the case of the remnant modeling. At each epoch, we estimate the total mass of dust in the shell as

$$M_d = \frac{4\pi\tau_V R_{in}^2 Y}{\kappa_d} r_{dg} \quad (\text{S1})$$

where R_{in} is the radius of the inner shell, $\kappa_d \approx 50 \text{ cm}^2 \text{ g}^{-1}$ is the average visual opacity per unit total mass (gas and dust) and $r_{dg} \approx 0.01$ is the dust-to-gas mass ratio (99). Adopting $Y = 10$ and $\kappa_d = 50 \text{ cm}^{-2} \text{ g}^{-1}$, we find

$$M_d \approx 6.1 \times 10^{-8} M_\odot \left(\frac{R_{in}}{1000 R_\odot} \right)^2 \tau_V \quad (\text{S2})$$

The evolution of the dust temperature, inner radius, inner source temperature and inferred photospheric radius are shown in Figure 3, while the evolution of the dust optical depth and total mass are shown in Figure S3. The evolution of the total source luminosity during this time is shown in Figure 4. In addition, to roughly estimate the source luminosity evolution between the end of the Gaia coverage and the remnant in 2022, we estimate a bolometric correction between the MIR luminosity estimated from trapezoidal integration of the NEOWISE fluxes and the total luminosity derived from the DUSTY analysis for the last Gaia + NEOWISE epoch. We apply this bolometric correction to the continuous NEOWISE MIR coverage in the gap, and show the estimated bolometric luminosity as hollow circles in Figure 4.

The analysis reveals a gradual increase in the dust temperature and a decrease in the inner shell radius and total luminosity, evolving to the remnant in 2022. A similar trend is seen in the evolution of the stellar temperature and radius, with the current remnant having a higher inferred temperature and smaller radius of $\approx 20\%$ that of the progenitor star. We can compare the evolution of the dust shell radius to the minimum radius at which dust can exist around the luminous star, i.e. the dust condensation radius, given by (16)

$$r_c \approx 11 \text{ AU} \left(\frac{L}{10^5 L_\odot} \right)^{1/2} \left(\frac{1500 \text{ K}}{T_d} \right)^2 Q_{rat}^{-1/2} \quad (\text{S3})$$

where r_c is the condensation radius, L is the source luminosity and Q_{rat} is the ratio of Planck-averaged absorption efficiency of the dust to the stellar photosphere. For $T_d \approx 1500 \text{ K}$ and $T_* \approx$

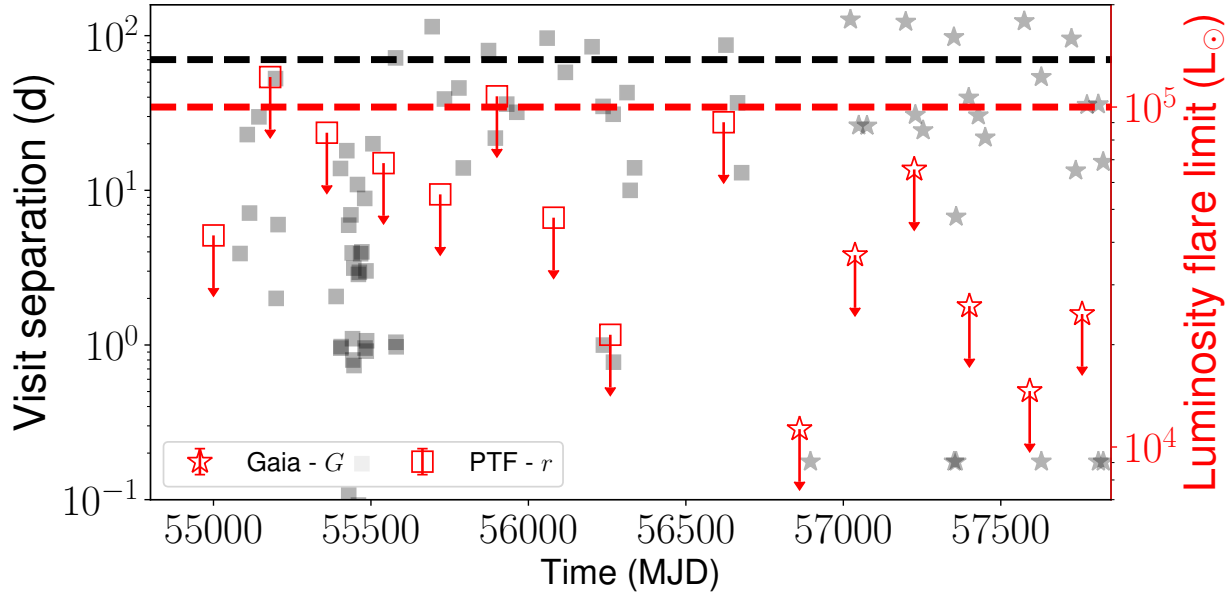


Figure S4: Constraints on the peak luminosity and timescale of an optical outburst in M31-2014-DS1. The left axis (gray squares and stars) shows the time separation between successive observations of the source in PTF r -band and Gaia data. The right axis (red squares and stars) indicates upper limits on the luminosity of an optical outburst accounting for the irregular variability of the star. The black and red dashed lines show our adopted upper limits on the timescale and luminosity of a missed outburst.

5000 K, we estimate $Q_{rat} \approx 0.15$, resulting in

$$r_c \approx 28 \text{ AU} \left(\frac{L}{10^5 L_\odot} \right)^{1/2} \left(\frac{1500 \text{ K}}{T_d} \right)^2 \quad (\text{S4})$$

Therefore, the observed progressive contraction of the inner shell radius to $\lesssim 40$ AU can be attributed to new dust formation near the condensation radius that causes the apparent shell to recede in radius from the progenitor circumstellar shell. While the optical depth of the dust shell increases dramatically (by $\gtrsim 10\times$) due to the gradual contraction of the shell, the total dust mass remains roughly constant in the initial ≈ 1000 d before increasing by $\approx 10^{-4} M_\odot$ during the subsequent period as the source evolves to the present day remnant.

Constraints on mass ejection

We use the continuous optical photometric coverage of M31-2014-DS1 between 2010 and 2020 by PTF and Gaia to place limits on an optical outburst, as expected for H-recombination powered

transients in failed SNe (13). While the progenitor is historically known, and detected as an irregular variable star in PTF and Gaia data (Figure 1), its light curve does not show an obvious optical outburst. To quantify the constraints on the timescale of a possibly missed outburst, we measure the difference between successive observations of the star in PTF *r*-band and Gaia *G*-band data, which provide the best temporal sampling, and show them in Figure S4 over the time span of the data set. Since no outburst (i.e. a brightening substantially exceeding the stellar variability) is nominally detected, we conservatively adopt an upper limit on the rise timescale of the outburst as half of the maximum visit separation during this time period (≈ 140 d). As the source exhibits irregular variability which can hide a possible low amplitude outburst, we measure the standard deviation of the flux variability over six-month bins, and adopt a conservative upper limit on the luminosity of a missed outburst as 10σ deviation from the median luminosity of the source in these bins (Figure S4). We adopt half of the maximum flare luminosity limit during this period ($\approx 10^5 L_\odot$) as an upper limit on the luminosity of a possible missed optical outburst in M31-2014-DS1. The constraints on the outburst luminosity and timescale are shown in Figure 4.

Stellar mass shock-heated and expelled in a full or partial stellar explosion expands, cools, and radiates as it becomes transparent, yielding transient but luminous emission. In the case of hydrogen-rich ejecta like that of type II supernovae, stellar merger ejecta, or weak explosions of massive stars, much of the appearance of these sources is modulated by the recombination of hydrogen at temperatures of a few to ten thousand Kelvin. As a result of this similarity, widely used scaling relations provide a relatively accurate representation of the characteristic timescale, color, and luminosity of such H-rich ejecta, though we note that in more detail, there is dependence upon the stellar model and shock passage through the star (100, 101). In particular, because the infall, shock passage, and reversal of material happen over one to several stellar dynamical times, we might expect transients that are broader but less luminous than their fully impulsive counterparts (12). With these caveats in mind, we nonetheless adopt the model of Kleiser et al. (2014)'s (equations 13 and 14) (102), which are

$$L_{\text{pl}} \approx 1.2 \times 10^{42} \text{ erg s}^{-1} \times E_{51}^{5/6} M_{10}^{-1/2} R_{500}^{2/3} \kappa_{0.4}^{-1/3} T_{6000}^{4/3}, \quad (\text{S5})$$

where L_{pl} is the transient's plateau luminosity, and

$$t_{\text{pl}} \approx 120 \text{ d} \times E_{51}^{-1/6} M_{10}^{1/2} R_{500}^{1/6} \kappa_{0.4}^{1/6} T_{6000}^{-2/3}, \quad (\text{S6})$$

where t_{pl} is the plateau duration. In both of the above expressions, E_{51} is the outburst energy in units of 10^{51} erg, M_{10} is the ejecta mass in units of $10 M_{\odot}$, R_{500} is the progenitor radius in units of $500 R_{\odot}$, $\kappa_{0.4}$ is the characteristic opacity before recombination in units of $0.4 \text{ cm}^2 \text{ g}^{-1}$, and T_{6000} is the effective temperature at which the recombining material becomes transparent, in units of 6000 K.

We apply this model to map out the range of transient durations and luminosities in Figure 4. The escape velocity of a $6M_{\odot}$, $500R_{\odot}$ progenitor star, as estimated from our SED modeling, is $\approx 70 \text{ km s}^{-1}$. We therefore adopt representative velocities for ejecta above these minimum escape speeds for different stellar models. Figure 4 shows tracks of $v_{\text{ej}} = 70, 350$ and 1750 km s^{-1} , with colors indicate different ejecta masses ranging from $10^{-2} M_{\odot}$ to $3 M_{\odot}$. Higher ejecta masses or faster velocities correspond to higher energy events that produce more luminous transients. The grey-shaded quadrant in Figure 4 (left panel) shows the parameter space of models that would have been detected given our constraints on the luminosity and duration of an outburst, and are therefore ruled out. Since the allowed masses (e.g. $\lesssim 0.1 M_{\odot}$ ejected at 70 km s^{-1} or $\lesssim 1 M_{\odot}$ ejected at 1750 km s^{-1}) are much less than the mass of our progenitor model ($\approx 6 M_{\odot}$ at the terminal stage), we conclude that the vast majority of the stellar material imploded, forming a new BH.

Stellar models, injection with shocks, and fallback

To model the implosion of a stellar envelope and the resulting accretion rate onto a newly-formed central compact object, we create models of the progenitor using the stellar evolution code MESA (25). MESA solves the equations of hydrostatic stellar structure and evolves them forward in time by computing the nuclear and thermal time-evolution of a star. These models inform us about the interior density profile of the progenitor star of M31-2014-DS1. By adjusting the model parameters, we create two qualitatively different models that share the approximate luminosity and effective temperature of the observed progenitor. Both models are evolved from the zero-age main sequence until carbon core depletion. From carbon core depletion, additional burning stages continue in the core, but without dramatic effect on the envelope structure that we are accessing with these models.

In the first case, we apply a higher-than-usual stellar wind mass loss rate throughout an initially $20.5 M_{\odot}$ star's evolution. Our model adopts a heavy element mass fraction of $Z = 0.02$. This model reaches carbon core depletion with a low-mass hydrogen envelope. We apply MESA's 'Dutch' wind

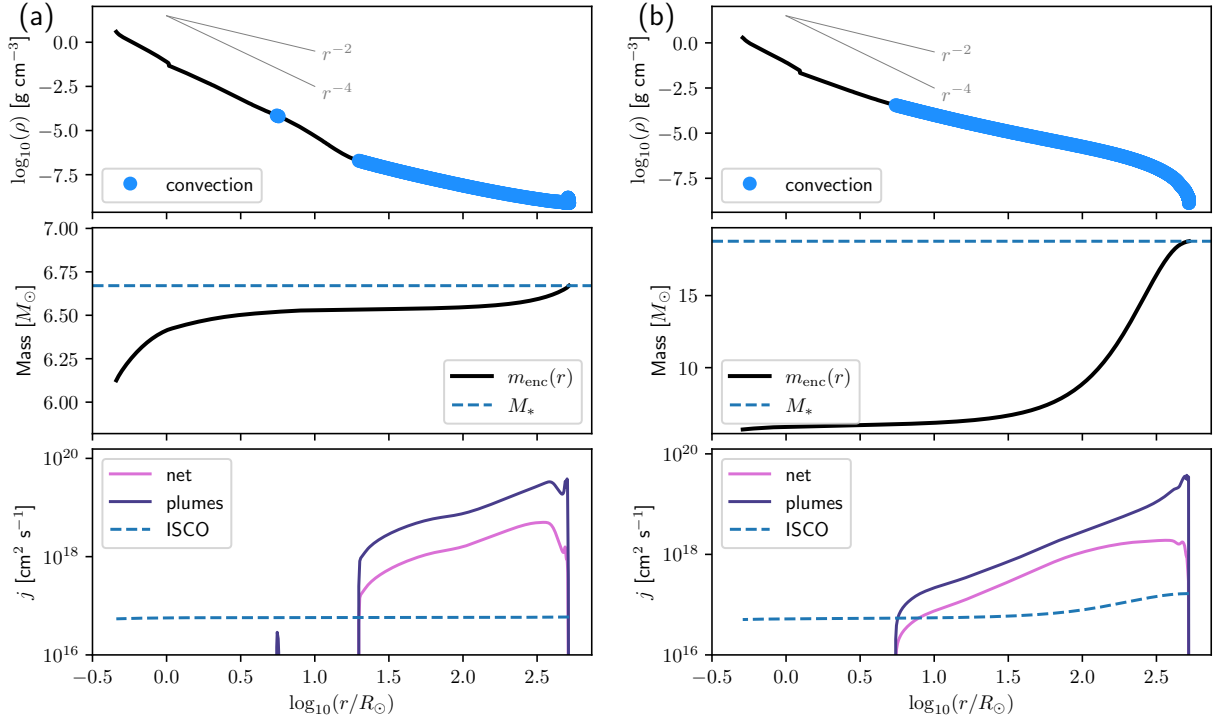


Figure S5: Comparison of the hydrogen envelope structures of a H-poor progenitor star model (a) and a H-rich counterpart of similar luminosity and effective temperature (b). The upper panels show the envelope density profile, with convective regions highlighted. The center panels compare the enclosed mass profiles, and the lower panels show the angular momentum content of the envelopes. In the upper and center panels we see that the H-rich envelope has a more extended convection zone, and thus carries more of its (overall greater) mass at large radii. The H-poor profile is, by comparison, much more centrally concentrated. The lower panels show the typical specific angular momentum of convective plumes as compared to the mean angular momentum of convective shells, and to the innermost stable circular orbit if all of the enclosed mass were to collapse to a BH. These profiles show that convective regions carry much more random angular momentum than a BH horizon, preventing direct fallback of these outer envelope regions.

scheme, appropriate for massive stars, with a slightly elevated coefficient of $\eta_{\text{wind}} = 3.75$ (relative to $\eta_{\text{wind}} \sim 1$). As it evolves, its colors remain red ($T_{\text{eff}} \sim 3500 - 3600$ K) until the H envelope decreases to less than a solar mass. At this point, the envelope begins to shrink and become hotter, and the star appears more blue than a typical red giant. Near carbon core depletion, our model has a luminosity of $L \approx 10^5 L_{\odot}$, an effective temperature of $T_{\text{eff}} = 4500$ K, and a radius of $R = 516 R_{\odot}$. The interior structure of the hydrogen envelope of these models is shown in Figure S5. We note that if a star had lost its mass instead through mass transfer in a binary system its structure would be similar.

In the second case, we evolve an initially $19M_{\odot}$ star from zero age main sequence until carbon core depletion. We match the approximate colors of the progenitor not by applying a stellar wind, but by adjusting the mixing length parameter of the stellar envelope's convection. A nominal value is $\alpha_{\text{mlt}} \sim 1 - 3$. We apply $\alpha_{\text{mlt}} = 3.5$, which moves the star's Hayashi track evolution to colors consistent with the M31-2014-DS1 progenitor and with our H-depleted progenitor. We consider this model less physical than the hydrogen-depletion scenario. In particular, were all stars to share this property, red giant and supergiant stars would not have their low effective temperatures of a few thousand Kelvin. However, this approach lets us create a H-rich stellar envelope that can be directly compared to our previous case, isolating the difference in stellar interior structure as opposed to overall radius (Figure S5). At carbon core depletion, the H-rich model has a luminosity of $L_* \approx 10^5 L_{\odot}$, an effective temperature of $T_{\text{eff}} = 4500$ K, and a radius of $R_* = 523R_{\odot}$.

We adopt a simplified model for how energy is added to these stellar envelopes by an outgoing shock launched following the collapse of the core. The physics of shock energy deposition in failed supernovae is complex. It depends not just on outward shock propagation through the infalling stellar material (14, 103), but also on the time-dependence of collapse of the core into a proto-neutron star (15), and on possible flow reversal and feedback from inefficient accretion onto a newly formed compact object (8, 9) (11, 12). The full scope of these theoretical considerations adds a level of specificity beyond the scope of our study. For qualitative purposes, we examine a model in which kinetic energy is added to stellar layers following a simple, power-law prescription, as adopted by Quataert & Kasen (2012) (37),

$$v_{\text{sh}} = v_0 \left(\frac{r}{R_*} \right)^{\alpha} \quad (\text{S7})$$

We integrate this profile over the stellar envelope to obtain the energy added,

$$E_{\text{sh}} = \int_0^{R_*} 2\pi r^2 \rho v_{\text{sh}}^2 dr, \quad (\text{S8})$$

and vary v_0 to achieve the desired shock energy deposition, E_{sh} . A fluid parcel thus initially is launched outward but may reverse and fall back if v_{sh} is less than the local escape velocity. The fallback time for a given shell of bound stellar material at initial radius r can be estimated as

$$t_{\text{fb}}(r) = \left(1 + \frac{v_{\text{sh}}(r)}{v_{\text{esc}}(r)} \right) t_{\text{ff}}(r) \quad (\text{S9})$$

where $v_{\text{esc}}(r) = (2Gm/r)^{1/2}$, m is the mass enclosed within radius r , and

$$t_{\text{ff}}(r) = \pi \left(\frac{r^3}{8Gm} \right)^{1/2}. \quad (\text{S10})$$

Thus, when $v_{\text{sh}} = 0$, the fallback time reduces to t_{ff} . The mass fallback rate is $\dot{M} = dm_{\text{shell}}/dt_{\text{fb}}$. At late times, when marginally bound material falls back, the asymptotic fallback rate is

$$\dot{M} \approx \frac{2\pi}{3} r_0^2 \rho(r_0) v_{\text{esc}}(r_0) \left(\frac{t}{t_{\text{ff}}(r_0)} \right)^{-5/3}, \quad (\text{S11})$$

where r_0 and the quantities that depend on it are evaluated at the critical radius where the shock velocity equals the escape velocity $v_{\text{sh}}(r_0) = v_{\text{esc}}(r_0)$. The unbound mass is material with $v_{\text{sh}}(r_0) > v_{\text{esc}}(r_0)$, or

$$m_{\text{ej}} = \int_{r_0}^{R_*} 4\pi r^2 \rho dr. \quad (\text{S12})$$

When random angular momentum is present in the turbulently convective envelopes of supergiant stars, this can lead to significant departures from spherical collapse (8–12). Individual plumes of stellar material have a broad, isotropic angular momentum distribution with characteristic amplitude of

$$j_{\text{plumes}} \approx r v_{\text{conv}} \quad (\text{S13})$$

where v_{conv} is the typical convective velocity at radius r and is a prediction of the mixing length theory applied in stellar models. These plumes, if they freefall, become rotationally supported at

$$r_{\text{circ}} \approx \frac{j_{\text{plumes}}^2}{GM}. \quad (\text{S14})$$

By comparison the angular momentum of the innermost stable circular orbit is approximately (depending on the BH's spin)

$$j_{\text{isco}} \approx \frac{2GM_{\text{bh}}}{c}. \quad (\text{S15})$$

The ratio of circularization radius to innermost stable circular orbit is

$$\frac{r_{\text{circ}}}{r_{\text{isco}}} \approx \left(\frac{j_{\text{plumes}}}{j_{\text{isco}}} \right)^2. \quad (\text{S16})$$

Below this radius the continued infall is turbulence dominated. As a result, the amount of mass that makes it inward is a function of radius, with turbulent convective motion preventing some degree of infall. The accretion rate through radius r can be parameterized

$$\dot{m} \approx \dot{m}(r_{\text{circ}}) \left(\frac{r}{r_{\text{circ}}} \right)^\beta \quad (\text{S17})$$

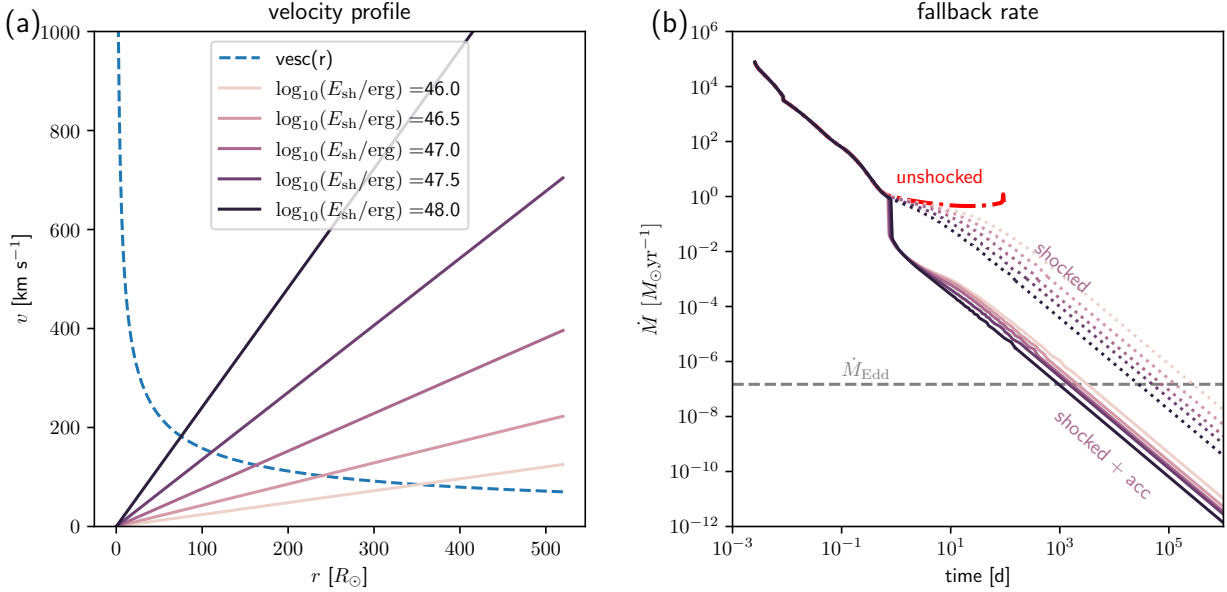


Figure S6: Shock velocity profiles (a) and the resulting fallback rate curves (b). For a range of shock energies we show how our linear velocity profile compares to the local escape velocity. Regions with $v_{\text{sh}} > v_{\text{esc}}(r)$ yield unbound material, while regions with $v_{\text{sh}} < v_{\text{esc}}(r)$ fall back. The deposition of shock energy yields long, $\dot{m} \propto t^{-5/3}$ tails in the fallback rate, that are generated from marginally bound material with $v_{\text{sh}} \sim v_{\text{esc}}(r)$. (b) compares the unshocked fallback profile to the fallback rate of shocked material (dotted lines) and the rate inferred to accrete onto the BH after accounting for the angular momentum barrier of the initial convective envelope (solid lines, labeled “shocked + acc”).

where β is a power on the order of 0.5 plus or minus a few tenths. In generalized simulations of turbulent infall Xu et al (40) derived $\beta \approx 0.7$ for a $\gamma = 5/3$ gas, while Antoni and Quataert (11) found $\beta \approx 0.6$ in their simulations of red supergiant collapse. We adopt that second value here. Thus, our expression for the mass accreted onto the newly-formed BH is

$$\dot{m}_{\text{BH}} \approx \dot{m}(r_{\text{circ}}) \left(\frac{r_{\text{isco}}}{r_{\text{circ}}} \right)^{0.6}. \quad (\text{S18})$$

To compute the emergent luminosity from the accretion process in the late-time evolution, we adopt a simple radiative efficiency $\eta = 0.05$ to convert from the rest mass energy of the accreted material ($L = \eta \dot{m} c^2$).

Figure S6 illustrates the shock-injection, fallback, and accretion model applied to the H-poor progenitor model for a range of typical shock energies that might be realized in the collapse of a proto-NS to a BH (15). Sufficiently large energies generate unbound material, and spread gas into

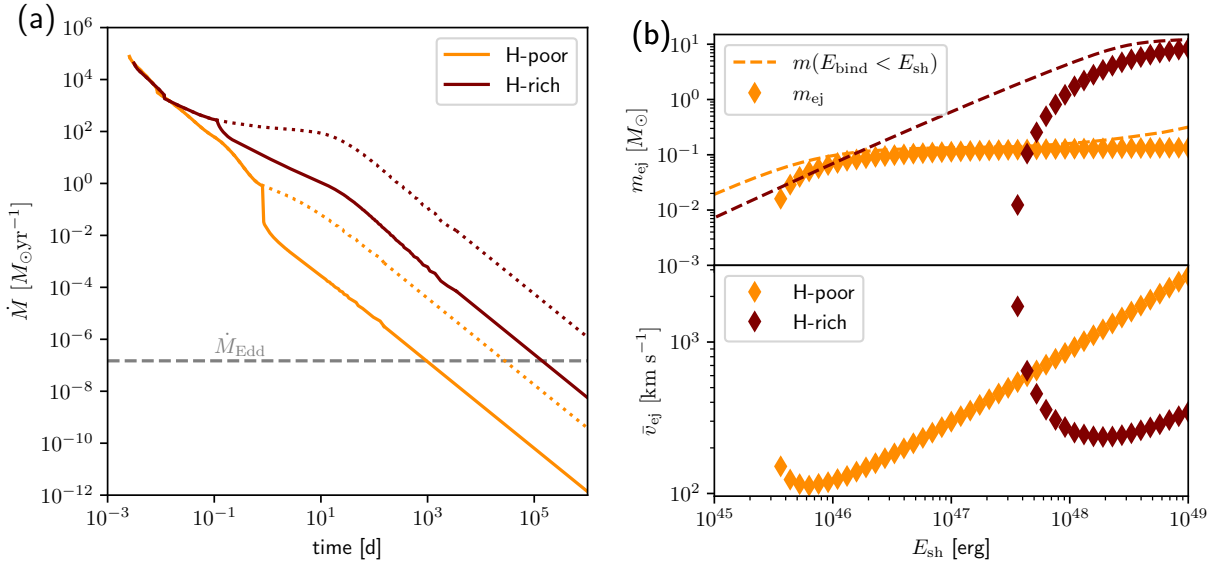


Figure S7: A comparison of fallback (a) and mass ejection (b) in H-rich and H-poor progenitor models. Where solid and dashed lines in panel (a) have the same meaning as Figure S6. In the H-poor case, the BH accretion drops below the BH Eddington limit at $\sim 10^3$ d. In the H-rich case, this transition extends to $\sim 10^5$ d. The H-poor model yields $\sim 0.1 M_{\odot}$ of ejecta with a typical velocity of hundreds of km s $^{-1}$ at typical shock energies while the H-rich model ejects several solar masses of material at somewhat lower velocities. They yield transient events with duration of tens of days in the case of the H-poor envelope or hundreds of days for the H-rich envelope. Because the accretion rate drops below Eddington at $\sim 10^3$ d and hundred-day recombination transients are strongly ruled out in our data, we suggest that the collapse of a H-poor star is most consistent with our data.

marginally-bound trajectories that add a late-time $t^{-5/3}$ asymptotic fallback. The effect of angular momentum (in the model labeled “shocked + acc”) is to greatly reduce the accretion efficiency, such that the BH accretion rate drops below its Eddington limit after about 10^3 d post-collapse for shock energies in the range of 10^{46} to 10^{48} erg. The difference between the “shocked” and “shocked + acc” traces \dot{M}_{ej} , the rate at which material is ejected rather than being accreted. The bulk of the mass is expelled in the tens - thousand day range.

Figure S7 compares fallback and mass ejection that is projected for the H-rich and H-poor progenitor models. In the H-rich case, the late-time fallback from the mass-rich envelope is dramatically elevated (above the Eddington limit for 10^5 d ~ 300 yr). By contrast, the centrally concentrated H-poor model mostly accretes early, and drops below the Eddington limit in just a few years. The expected ejecta properties also diverge. The H-rich model yields several solar masses of ejecta and transients of $L > 10^6 L_{\odot}$ for hundreds of days. The H-poor model, by contrast ejects about $0.1 M_{\odot}$

at a higher velocity of several hundred km s⁻¹. We show the expected luminosity and timescale for the resulting outbursts (for H-recombination powered events) in Figure 4, demonstrating that the transient would last tens of days. Therefore, these brief transients could be missed without high-cadence optical monitoring.

Physical limits from X-ray non-detection

The accretion of the turbulent convective envelope onto the black hole is inefficient, leading the vast majority of the outer envelope material to be expelled (as highlighted by the difference between the dotted “shocked” and solid “shocked + acc” lines) (12). In principle, obscuration of the central, newly-formed BH comes from both ejected and bound material. We estimate that the column depth of hydrogen as follows. The unbound component with $v_{\text{sh}} > v_{\text{esc}}$ is assumed to continue to expand at constant velocity, such that its radius is $v_{\text{sh}}t$. Each radial zone in the initial stellar structure has mass dm . Then,

$$N_{\text{H,ej}} \approx \frac{1}{m_p} \int \frac{dm}{4\pi(v_{\text{sh}}t)^2} \quad (\text{S19})$$

which scales as t^{-2} . The initially bound component that falls back toward the newly-formed black hole contains both the small fraction of material that successfully accretes and the majority that is expelled instead. Though it may be quite dependent on feedback from the passing shock (12), we crudely estimate the column of un-accreted material as a function of time. Most of the infall reverses around a scale of r_{circ} , and expands from there. We estimate that the fallback driven outflow produces a column on the order of

$$N_{\text{H,wind}} \sim \frac{1}{m_p} \frac{\dot{m}(r_{\text{circ}})}{4\pi r_{\text{circ}} v_{\text{esc}}(r_{\text{circ}})} \quad (\text{S20})$$

This component scales with the fallback rate, and therefore decays as $t^{-5/3}$ at late times. Thus, the ejecta column dissipates fastest, and at late times remaining column density will depend on the particulars of the inefficient accretion-and-outflow process.

Figure S8 estimates the column density as a function of time from our model. This includes both the unbound and reversing-fallback (labeled “accretion outflow”) components. At late time, the more uncertain accretion outflow component appears to be most important, due to its shallower time decay. We see that for typical energies the H number density along the line of sight drops below

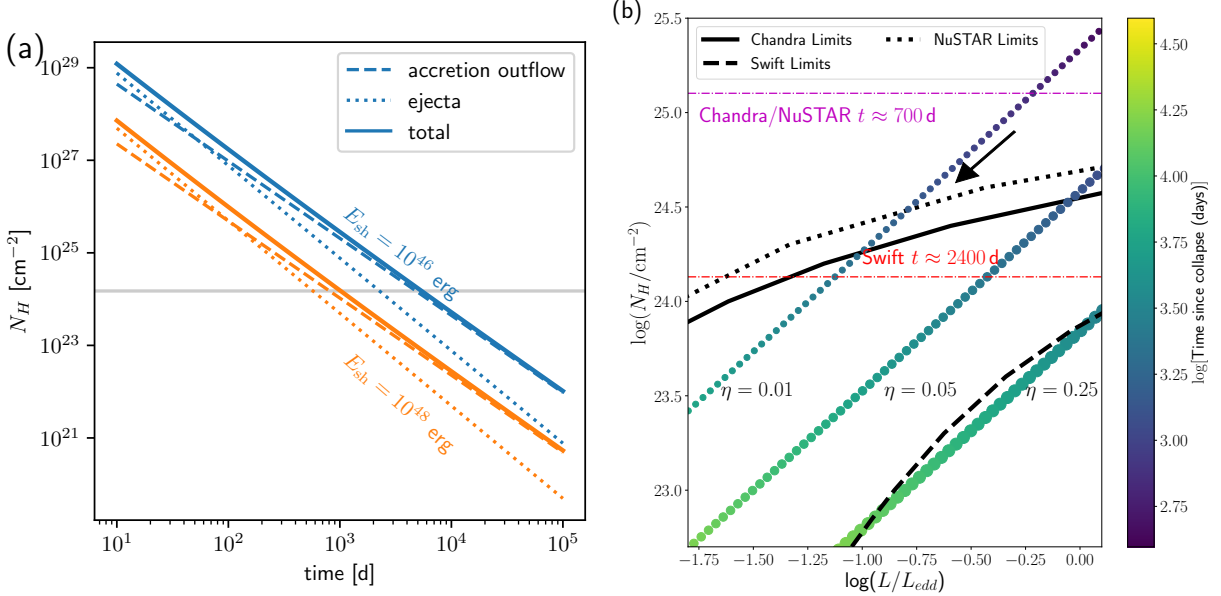


Figure S8: Predicted hydrogen column density surrounding a newborn BH for different shock energies (a) and the evolution of the column density and emergent luminosity as a function of time (b). (a) We show the contribution from the expanding ejecta, which decays as t^{-2} and that from the reversal of material falling back with excess of angular momentum, which decays with the fallback rate, as $t^{-5/3}$. For reasonable shock energies, the line of sight to the source could become transparent ($N_H \lesssim 1.5 \times 10^{24}$ cm $^{-2}$, shown as gray horizontal line, corresponding to Thompson optical depth of less than unity) to soft X-rays in the few $\times 10^3$ d to 10^4 d time range. (b) We show the evolution of the column density as a function of the accretion luminosity (normalized to the Eddington luminosity of a $5 M_\odot$ BH) for $E_{sh} = 10^{47}$ erg, with the symbol colors indicating progression of time (shown with an arrow) for three different radiative efficiencies ($\eta = 0.01, 0.05, 0.25$). The magenta dot-dashed and red dashed lines show the estimated N_H from the model at the epoch of the archival Chandra/NuSTAR (end of 2015) and Swift X-ray observations, respectively. The black solid, dotted and dashed lines show the detection threshold for X-ray emission for the respective Chandra, NuSTAR and Swift X-ray observations, where only regions below the lines would be detectable in the data – demonstrating that the lack of an X-ray detection can be explained by heavy obscuration in both observations.

10^{24} cm $^{-2}$ – the approximate level to allow soft X-rays to penetrate – in the range of a few $\times 10^3$ to 10^4 d. To quantitatively compare against our observations, we can track the expected evolution of our model as a function of the surrounding column density and accretion luminosity (both of which decrease rapidly with time), as shown in Figure S8. For comparison, we also show the estimated total N_H at the epochs of the archival Chandra, NuSTAR and Swift X-ray observations together with the phase space of N_H and L that are ruled out by the X-ray non-detection (assuming a $\Gamma = 2$ intrinsic X-ray spectrum). The models consistently suggest that the source was too heavily obscured

at the epochs of the archival X-ray observations, but that X-ray monitoring of the nascent BH in the coming years may provide a clearing view of the declining accretion onto the newly-formed BH.

Supplementary Text

The case of NGC 6946-BH1

M31-2014-DS1 shares several similarities with a previously reported failed SN candidate NGC 6946-BH1 (41–43) – in its luminous supergiant progenitor, bolometric decay and a remnant dominated by infrared emission. While its progenitor was suggested to be a red supergiant based on a comparison of its colors to single stellar evolutionary tracks (42), its pre-outburst colors were potentially consistent with a hydrogen depleted yellow supergiant as well (46). To make quantitative comparisons against our analysis for M31-2014-DS1, we followed the same analysis chain for this object by producing a stellar model that matches the luminosity and temperature of its progenitor, shown in Figure 2. We find a good match to the properties with an initial mass of $\approx 28 M_{\odot}$ that retains only $\approx 1.4 M_{\odot}$ of its H envelope and a final mass of $\approx 9.9 M_{\odot}$. We show its internal structure in Figure S9.

As in the case of modeling M31-2014-DS1, we investigate the outburst properties for this model as a function of the input shock energy produced from neutrino mass loss. Figure S9 shows that the higher hydrogen envelope mass and larger radius for this stellar model results in the ejection of a larger amount of mass (few $\times 0.1 M_{\odot}$) at higher velocities (few $\times 100 \text{ km s}^{-1}$) for this model, compared to the case of M31-2014-DS1. The associated outburst properties associated with H-recombination for the ejecta are shown in Figure S10, compared to the favored H-poor and unlikely H-rich progenitor model for M31-2014-DS1. Figure S10 shows that the larger ejecta mass in this case produces a typically longer duration outburst than the H-poor model for M31-2014-DS1. In the case of NGC 6946-BH1, the total duration of the outburst was poorly constrained between 3 and 11 months (42). Taking the rise time of the outburst to be half of the total duration, we show in Figure S10 that the observed outburst properties of the source are consistent with a $\sim 10^{47} \text{ erg}$ shock powered by neutrino mass loss.

As the loosely bound material falls back into the stellar core in this case, Figure S10 shows the evolution of the mass fallback rate as a function of time. While the $\approx 5\times$ more massive H-envelope

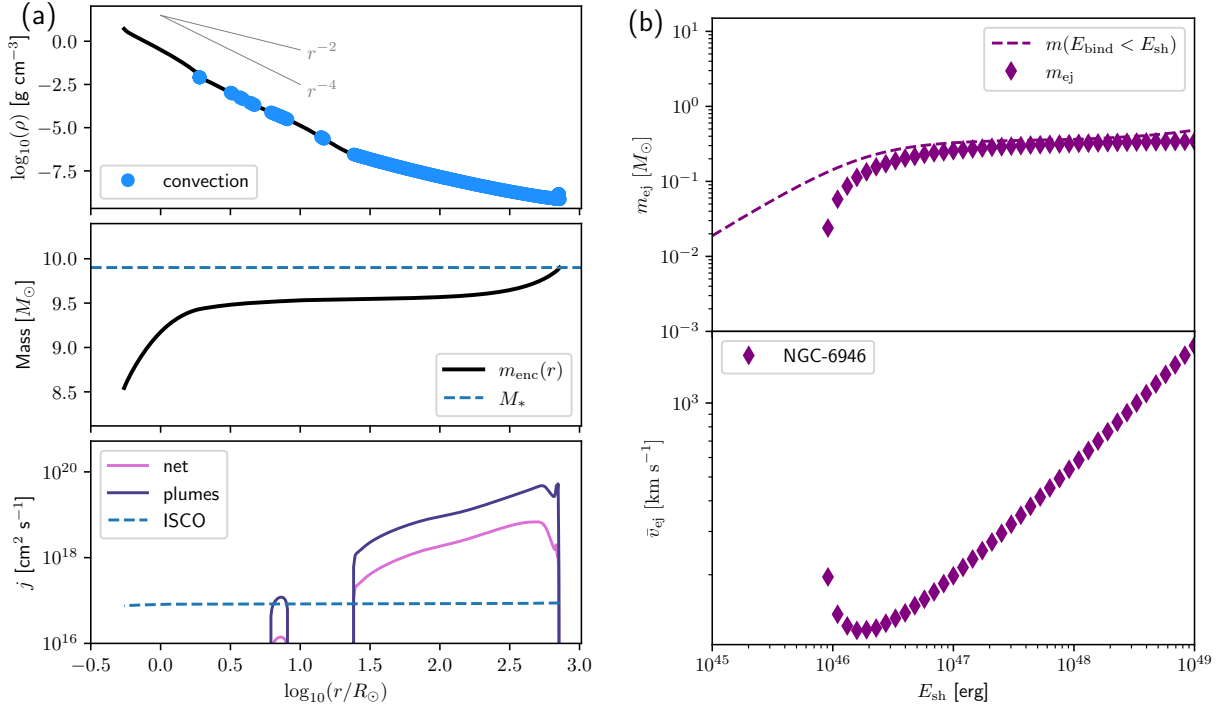


Figure S9: A stellar model and associated outburst properties for the progenitor of NGC 6946-BH1. (a) Same as Figure S5 for the NGC 6946-BH1 terminal stellar model (luminosity and temperature shown in Figure 2. (b) The ejecta mass and velocity for the NGC 6946-BH1 stellar model as a function of the neutrino mass loss shock energy, as in Figure S7.

for this model leads to a marginally longer time of ≈ 3000 d to fall below the Eddington rate, it similarly fades by $\approx 10\times$ over a few thousand days after the collapse of the core. NGC 6946-BH1 was reported to fade to $\sim 10\%$ of its progenitor luminosity in ~ 3000 d, and we compare its bolometric light curve (converted to effective mass accretion rate) to our model in Figure S10. Recently, observations of the remnant were reported with the JWST, showing that the remnant remains at a luminosity of $\sim 10 - 20\%$ of the progenitor (45, 47). Noting that the earlier epochs of observation did not have mid-IR coverage (and therefore the bolometric luminosity is not accurately constrained), the comparison demonstrates that the slow fading of NGC 6946-BH1 indicated by JWST data is consistent with the model – that predicts only modest luminosity fading (by a factor of ≈ 3) within the last decade.

Table S1: Multi-color photometry of M31-2014-DS1.

MJD	Flux (mJy)	Instrument	Filter
55211.233	0.979 ± 0.010	NEOWISE	W1
55398.412	1.034 ± 0.008	NEOWISE	W1
55575.174	0.967 ± 0.010	NEOWISE	W1
56674.192	0.984 ± 0.011	NEOWISE	W1
56860.963	1.095 ± 0.009	NEOWISE	W1
57037.092	1.051 ± 0.013	NEOWISE	W1
57225.124	1.160 ± 0.011	NEOWISE	W1
57400.316	1.100 ± 0.011	NEOWISE	W1
57591.789	1.345 ± 0.010	NEOWISE	W1
57758.220	1.514 ± 0.011	NEOWISE	W1
57956.318	1.435 ± 0.012	NEOWISE	W1
58120.287	0.849 ± 0.012	NEOWISE	W1
58320.502	0.787 ± 0.012	NEOWISE	W1
58480.931	0.568 ± 0.012	NEOWISE	W1
58686.176	0.645 ± 0.011	NEOWISE	W1
58848.318	0.422 ± 0.012	NEOWISE	W1
59051.860	0.442 ± 0.012	NEOWISE	W1
59212.180	0.302 ± 0.012	NEOWISE	W1
59415.952	0.355 ± 0.012	NEOWISE	W1
59576.493	0.221 ± 0.012	NEOWISE	W1
55211.233	1.014 ± 0.019	NEOWISE	W2
55398.412	1.081 ± 0.014	NEOWISE	W2
55575.174	0.922 ± 0.017	NEOWISE	W2
56674.192	0.943 ± 0.019	NEOWISE	W2
56860.930	0.996 ± 0.016	NEOWISE	W2
57037.092	1.132 ± 0.023	NEOWISE	W2

Table S1: Multi-color photometry of M31-2014-DS1 (Continued).

MJD	Flux (mJy)	Instrument	Filter
57225.124	1.064 ± 0.018	NEOWISE	W2
57400.316	1.122 ± 0.020	NEOWISE	W2
57591.789	1.252 ± 0.020	NEOWISE	W2
57758.220	1.441 ± 0.020	NEOWISE	W2
57956.318	1.246 ± 0.022	NEOWISE	W2
58120.287	0.730 ± 0.021	NEOWISE	W2
58320.502	0.613 ± 0.023	NEOWISE	W2
58480.931	0.587 ± 0.021	NEOWISE	W2
58686.176	0.520 ± 0.023	NEOWISE	W2
58848.318	0.502 ± 0.024	NEOWISE	W2
59051.860	0.399 ± 0.023	NEOWISE	W2
59212.180	0.435 ± 0.022	NEOWISE	W2
59415.887	0.371 ± 0.027	NEOWISE	W2
59576.493	0.338 ± 0.021	NEOWISE	W2
56895.413	0.109 ± 0.001	Gaia	<i>G</i>
56895.590	0.111 ± 0.002	Gaia	<i>G</i>
57022.569	0.254 ± 0.001	Gaia	<i>G</i>
57022.643	0.251 ± 0.002	Gaia	<i>G</i>
57048.881	0.222 ± 0.001	Gaia	<i>G</i>
57075.050	0.259 ± 0.001	Gaia	<i>G</i>
57075.124	0.253 ± 0.001	Gaia	<i>G</i>
57198.047	0.112 ± 0.001	Gaia	<i>G</i>
57228.788	0.101 ± 0.001	Gaia	<i>G</i>
57228.862	0.106 ± 0.001	Gaia	<i>G</i>
57253.286	0.212 ± 0.002	Gaia	<i>G</i>
57253.360	0.215 ± 0.002	Gaia	<i>G</i>

Table S1: Multi-color photometry of M31-2014-DS1 (Continued).

MJD	Flux (mJy)	Instrument	Filter
57351.155	0.091 ± 0.001	Gaia	<i>G</i>
57351.229	0.092 ± 0.001	Gaia	<i>G</i>
57351.406	0.092 ± 0.001	Gaia	<i>G</i>
57351.480	0.093 ± 0.001	Gaia	<i>G</i>
57358.233	0.063 ± 0.001	Gaia	<i>G</i>
57358.409	0.061 ± 0.001	Gaia	<i>G</i>
57398.115	0.059 ± 0.001	Gaia	<i>G</i>
57428.597	0.093 ± 0.001	Gaia	<i>G</i>
57428.671	0.096 ± 0.001	Gaia	<i>G</i>
57450.598	0.047 ± 0.001	Gaia	<i>G</i>
57450.672	0.047 ± 0.001	Gaia	<i>G</i>
57574.597	0.057 ± 0.001	Gaia	<i>G</i>
57574.671	0.059 ± 0.001	Gaia	<i>G</i>
57628.656	0.075 ± 0.001	Gaia	<i>G</i>
57628.832	0.074 ± 0.001	Gaia	<i>G</i>
57724.444	0.045 ± 0.001	Gaia	<i>G</i>
57724.518	0.048 ± 0.001	Gaia	<i>G</i>
57737.947	0.083 ± 0.001	Gaia	<i>G</i>
57738.021	0.084 ± 0.001	Gaia	<i>G</i>
57773.662	0.089 ± 0.001	Gaia	<i>G</i>
57773.736	0.092 ± 0.002	Gaia	<i>G</i>
57809.697	0.077 ± 0.001	Gaia	<i>G</i>
57809.771	0.079 ± 0.001	Gaia	<i>G</i>
57809.947	0.074 ± 0.001	Gaia	<i>G</i>
57825.203	0.100 ± 0.002	Gaia	<i>G</i>
57825.277	0.099 ± 0.002	Gaia	<i>G</i>

Table S1: Multi-color photometry of M31-2014-DS1 (Continued).

MJD	Flux (mJy)	Instrument	Filter
57825.453	0.098 ± 0.001	Gaia	<i>G</i>
57825.527	0.099 ± 0.001	Gaia	<i>G</i>
57897.035	0.023 ± 0.001	Gaia	<i>G</i>
57897.211	0.023 ± 0.001	Gaia	<i>G</i>
57897.285	0.021 ± 0.001	Gaia	<i>G</i>
56895.414	0.041 ± 0.004	Gaia	<i>BP</i>
56895.590	0.043 ± 0.005	Gaia	<i>BP</i>
57022.570	0.113 ± 0.005	Gaia	<i>BP</i>
57022.644	0.138 ± 0.005	Gaia	<i>BP</i>
57075.050	0.128 ± 0.005	Gaia	<i>BP</i>
57075.124	0.120 ± 0.006	Gaia	<i>BP</i>
57198.047	0.018 ± 0.005	Gaia	<i>BP</i>
57198.121	0.015 ± 0.005	Gaia	<i>BP</i>
57228.789	0.027 ± 0.004	Gaia	<i>BP</i>
57228.863	0.028 ± 0.005	Gaia	<i>BP</i>
57253.287	0.070 ± 0.007	Gaia	<i>BP</i>
57253.361	0.067 ± 0.006	Gaia	<i>BP</i>
57351.156	0.027 ± 0.004	Gaia	<i>BP</i>
57351.230	0.032 ± 0.004	Gaia	<i>BP</i>
57351.406	0.048 ± 0.004	Gaia	<i>BP</i>
57351.480	0.016 ± 0.004	Gaia	<i>BP</i>
57358.233	0.412 ± 0.006	Gaia	<i>BP</i>
57358.409	0.007 ± 0.005	Gaia	<i>BP</i>
57398.116	0.012 ± 0.004	Gaia	<i>BP</i>
57428.598	0.036 ± 0.004	Gaia	<i>BP</i>
57428.672	0.028 ± 0.005	Gaia	<i>BP</i>

Table S1: Multi-color photometry of M31-2014-DS1 (Continued).

MJD	Flux (mJy)	Instrument	Filter
57450.672	0.001 ± 0.006	Gaia	<i>BP</i>
57574.597	0.002 ± 0.006	Gaia	<i>BP</i>
57574.671	0.001 ± 0.004	Gaia	<i>BP</i>
57628.656	0.020 ± 0.004	Gaia	<i>BP</i>
57628.832	0.013 ± 0.006	Gaia	<i>BP</i>
57737.948	0.006 ± 0.006	Gaia	<i>BP</i>
57738.022	0.024 ± 0.004	Gaia	<i>BP</i>
57773.662	0.018 ± 0.004	Gaia	<i>BP</i>
57773.736	0.013 ± 0.007	Gaia	<i>BP</i>
57809.697	0.023 ± 0.004	Gaia	<i>BP</i>
57809.771	13.890 ± 0.030	Gaia	<i>BP</i>
57809.947	0.019 ± 0.005	Gaia	<i>BP</i>
57825.203	0.024 ± 0.008	Gaia	<i>BP</i>
57825.277	0.017 ± 0.009	Gaia	<i>BP</i>
57825.453	0.037 ± 0.004	Gaia	<i>BP</i>
57825.527	0.009 ± 0.006	Gaia	<i>BP</i>
57897.211	0.003 ± 0.005	Gaia	<i>BP</i>
57897.285	0.011 ± 0.004	Gaia	<i>BP</i>
56895.414	0.220 ± 0.001	Gaia	<i>RP</i>
56895.590	0.232 ± 0.001	Gaia	<i>RP</i>
57022.570	0.478 ± 0.002	Gaia	<i>RP</i>
57022.644	0.435 ± 0.003	Gaia	<i>RP</i>
57075.051	0.461 ± 0.002	Gaia	<i>RP</i>
57075.125	0.451 ± 0.002	Gaia	<i>RP</i>
57198.048	0.232 ± 0.001	Gaia	<i>RP</i>
57198.122	0.218 ± 0.001	Gaia	<i>RP</i>

Table S1: Multi-color photometry of M31-2014-DS1 (Continued).

MJD	Flux (mJy)	Instrument	Filter
57228.789	0.218 ± 0.001	Gaia	<i>RP</i>
57228.863	0.232 ± 0.001	Gaia	<i>RP</i>
57253.287	0.452 ± 0.002	Gaia	<i>RP</i>
57253.361	0.419 ± 0.001	Gaia	<i>RP</i>
57351.156	0.238 ± 0.001	Gaia	<i>RP</i>
57351.230	0.185 ± 0.001	Gaia	<i>RP</i>
57351.406	0.201 ± 0.002	Gaia	<i>RP</i>
57351.480	0.195 ± 0.001	Gaia	<i>RP</i>
57358.233	0.150 ± 0.017	Gaia	<i>RP</i>
57358.410	0.131 ± 0.001	Gaia	<i>RP</i>
57398.116	0.167 ± 0.001	Gaia	<i>RP</i>
57428.598	0.737 ± 0.001	Gaia	<i>RP</i>
57428.672	0.212 ± 0.001	Gaia	<i>RP</i>
57450.672	0.123 ± 0.001	Gaia	<i>RP</i>
57574.597	0.103 ± 0.001	Gaia	<i>RP</i>
57574.671	0.129 ± 0.001	Gaia	<i>RP</i>
57628.656	0.176 ± 0.001	Gaia	<i>RP</i>
57628.832	0.179 ± 0.001	Gaia	<i>RP</i>
57737.948	0.202 ± 0.001	Gaia	<i>RP</i>
57738.022	0.273 ± 0.001	Gaia	<i>RP</i>
57773.662	0.198 ± 0.001	Gaia	<i>RP</i>
57773.736	0.193 ± 0.001	Gaia	<i>RP</i>
57809.697	0.173 ± 0.001	Gaia	<i>RP</i>
57809.771	0.194 ± 0.693	Gaia	<i>RP</i>
57809.948	0.172 ± 0.001	Gaia	<i>RP</i>
57825.203	0.244 ± 0.001	Gaia	<i>RP</i>

Table S1: Multi-color photometry of M31-2014-DS1 (Continued).

MJD	Flux (mJy)	Instrument	Filter
57825.277	0.206 ± 0.001	Gaia	<i>RP</i>
57825.453	0.227 ± 0.001	Gaia	<i>RP</i>
57825.527	0.232 ± 0.001	Gaia	<i>RP</i>
57897.212	0.066 ± 0.001	Gaia	<i>RP</i>
57897.286	0.074 ± 0.001	Gaia	<i>RP</i>
56269.196	0.161 ± 0.005	PTF	<i>r</i>
56269.231	0.162 ± 0.005	PTF	<i>r</i>
56337.119	0.156 ± 0.006	PTF	<i>r</i>
55403.320	0.264 ± 0.013	PTF	<i>r</i>
56269.107	0.157 ± 0.005	PTF	<i>r</i>
56270.191	0.169 ± 0.011	PTF	<i>r</i>
56269.202	0.162 ± 0.005	PTF	<i>r</i>
56269.229	0.160 ± 0.005	PTF	<i>r</i>
55463.262	0.209 ± 0.010	PTF	<i>r</i>
56269.175	0.155 ± 0.005	PTF	<i>r</i>
56270.213	0.171 ± 0.011	PTF	<i>r</i>
56269.241	0.164 ± 0.005	PTF	<i>r</i>
56323.102	0.166 ± 0.007	PTF	<i>r</i>
55485.115	0.161 ± 0.007	PTF	<i>r</i>
56117.425	0.179 ± 0.008	PTF	<i>r</i>
56237.080	0.169 ± 0.006	PTF	<i>r</i>
56270.132	0.173 ± 0.011	PTF	<i>r</i>
56270.185	0.172 ± 0.011	PTF	<i>r</i>
56269.182	0.160 ± 0.005	PTF	<i>r</i>
56270.216	0.170 ± 0.011	PTF	<i>r</i>
56270.220	0.165 ± 0.011	PTF	<i>r</i>

Table S1: Multi-color photometry of M31-2014-DS1 (Continued).

MJD	Flux (mJy)	Instrument	Filter
56270.229	0.177 ± 0.011	PTF	r
56269.201	0.156 ± 0.005	PTF	r
56269.225	0.159 ± 0.005	PTF	r
56269.230	0.158 ± 0.005	PTF	r
56269.235	0.167 ± 0.005	PTF	r
56269.243	0.159 ± 0.005	PTF	r
56269.303	0.158 ± 0.005	PTF	r
56323.143	0.162 ± 0.007	PTF	r
56337.149	0.151 ± 0.006	PTF	r
55793.257	0.239 ± 0.009	PTF	r
56269.297	0.158 ± 0.005	PTF	r
55387.415	0.419 ± 0.049	PTF	r
56313.105	0.183 ± 0.008	PTF	r
56270.159	0.164 ± 0.010	PTF	r
56270.145	0.167 ± 0.011	PTF	r
56270.152	0.170 ± 0.011	PTF	r
56269.169	0.160 ± 0.005	PTF	r
56269.213	0.155 ± 0.005	PTF	r
55436.435	0.234 ± 0.010	PTF	r
56269.228	0.164 ± 0.005	PTF	r
56270.154	0.166 ± 0.011	PTF	r
56270.182	0.174 ± 0.011	PTF	r
56270.188	0.171 ± 0.011	PTF	r
56270.198	0.178 ± 0.011	PTF	r
56269.184	0.161 ± 0.005	PTF	r
55963.105	0.375 ± 0.048	PTF	r

Table S1: Multi-color photometry of M31-2014-DS1 (Continued).

MJD	Flux (mJy)	Instrument	Filter
56270.212	0.166 ± 0.011	PTF	r
56269.185	0.154 ± 0.005	PTF	r
56270.078	0.165 ± 0.011	PTF	r
56270.104	0.181 ± 0.012	PTF	r
56270.119	0.169 ± 0.011	PTF	r
56270.144	0.176 ± 0.011	PTF	r
56270.162	0.172 ± 0.011	PTF	r
56270.161	0.167 ± 0.011	PTF	r
56270.186	0.168 ± 0.011	PTF	r
56269.190	0.166 ± 0.005	PTF	r
56270.232	0.171 ± 0.011	PTF	r
56269.212	0.162 ± 0.005	PTF	r
56270.251	0.169 ± 0.011	PTF	r
56269.234	0.171 ± 0.005	PTF	r
56269.165	0.155 ± 0.005	PTF	r
55404.343	0.243 ± 0.010	PTF	r
56270.184	0.164 ± 0.011	PTF	r
56270.118	0.177 ± 0.011	PTF	r
56269.237	0.164 ± 0.005	PTF	r
56269.254	0.163 ± 0.005	PTF	r
55080.457	0.263 ± 0.015	PTF	r
55442.322	0.357 ± 0.009	PTF	r
55481.189	0.165 ± 0.005	PTF	r
56117.395	0.170 ± 0.007	PTF	r
56238.079	0.178 ± 0.007	PTF	r
56269.171	0.160 ± 0.005	PTF	r

Table S1: Multi-color photometry of M31-2014-DS1 (Continued).

MJD	Flux (mJy)	Instrument	Filter
56323.110	0.170 ± 0.007	PTF	<i>r</i>
55463.218	0.199 ± 0.009	PTF	<i>r</i>
55460.132	0.318 ± 0.011	PTF	<i>r</i>
56270.120	0.171 ± 0.011	PTF	<i>r</i>
56270.111	0.163 ± 0.011	PTF	<i>r</i>
56270.147	0.174 ± 0.011	PTF	<i>r</i>
56269.167	0.155 ± 0.005	PTF	<i>r</i>
56269.192	0.159 ± 0.005	PTF	<i>r</i>
56323.122	0.161 ± 0.006	PTF	<i>r</i>
56540.474	0.352 ± 0.022	PTF	<i>r</i>
55484.202	0.143 ± 0.010	PTF	<i>r</i>
56270.101	0.173 ± 0.011	PTF	<i>r</i>
56270.149	0.169 ± 0.011	PTF	<i>r</i>
56270.177	0.178 ± 0.012	PTF	<i>r</i>
56269.159	0.163 ± 0.005	PTF	<i>r</i>
56270.199	0.175 ± 0.011	PTF	<i>r</i>
56269.227	0.165 ± 0.005	PTF	<i>r</i>
56270.269	0.166 ± 0.011	PTF	<i>r</i>
56269.247	0.170 ± 0.005	PTF	<i>r</i>
56677.108	0.162 ± 0.013	PTF	<i>r</i>
56270.113	0.173 ± 0.011	PTF	<i>r</i>
55733.414	0.285 ± 0.011	PTF	<i>r</i>
55199.085	0.425 ± 0.012	PTF	<i>r</i>
56270.112	0.174 ± 0.011	PTF	<i>r</i>
56270.117	0.178 ± 0.011	PTF	<i>r</i>
56269.155	0.153 ± 0.005	PTF	<i>r</i>

Table S1: Multi-color photometry of M31-2014-DS1 (Continued).

MJD	Flux (mJy)	Instrument	Filter
55440.375	0.307 ± 0.009	PTF	<i>r</i>
55580.170	0.216 ± 0.008	PTF	<i>r</i>
55578.155	0.122 ± 0.015	PTF	<i>r</i>
55446.257	0.181 ± 0.007	PTF	<i>r</i>
55471.326	0.143 ± 0.019	PTF	<i>r</i>
55144.319	0.423 ± 0.029	PTF	<i>r</i>
55404.274	0.251 ± 0.013	PTF	<i>r</i>
55436.437	0.244 ± 0.010	PTF	<i>r</i>
55441.474	0.345 ± 0.010	PTF	<i>r</i>
55480.188	0.179 ± 0.006	PTF	<i>r</i>
55471.155	0.173 ± 0.013	PTF	<i>r</i>
55873.316	0.260 ± 0.014	PTF	<i>r</i>
55486.267	0.173 ± 0.009	PTF	<i>r</i>
55442.273	0.352 ± 0.009	PTF	<i>r</i>
55460.225	0.293 ± 0.009	PTF	<i>r</i>
55460.268	0.304 ± 0.009	PTF	<i>r</i>
55429.312	0.254 ± 0.008	PTF	<i>r</i>
55485.159	0.156 ± 0.006	PTF	<i>r</i>
55405.319	0.297 ± 0.016	PTF	<i>r</i>
56664.110	0.179 ± 0.008	PTF	<i>r</i>
55080.371	0.255 ± 0.014	PTF	<i>r</i>
55114.421	0.265 ± 0.030	PTF	<i>r</i>
55107.293	0.319 ± 0.013	PTF	<i>r</i>
55442.378	0.360 ± 0.009	PTF	<i>r</i>
55895.077	0.129 ± 0.010	PTF	<i>r</i>
56269.163	0.157 ± 0.005	PTF	<i>r</i>

Table S1: Multi-color photometry of M31-2014-DS1 (Continued).

MJD	Flux (mJy)	Instrument	Filter
55446.267	0.173 ± 0.006	PTF	<i>r</i>
55694.477	0.194 ± 0.007	PTF	<i>r</i>
55467.154	0.117 ± 0.009	PTF	<i>r</i>
56269.168	0.152 ± 0.005	PTF	<i>r</i>
55389.474	0.563 ± 0.063	PTF	<i>r</i>
56269.210	0.154 ± 0.005	PTF	<i>r</i>
55442.361	0.353 ± 0.009	PTF	<i>r</i>
55436.432	0.241 ± 0.010	PTF	<i>r</i>
55144.275	0.441 ± 0.030	PTF	<i>r</i>
56059.490	0.094 ± 0.009	PTF	<i>r</i>
56269.250	0.165 ± 0.005	PTF	<i>r</i>
55446.289	0.184 ± 0.007	PTF	<i>r</i>
55931.148	0.332 ± 0.045	PTF	<i>r</i>
55486.224	0.166 ± 0.009	PTF	<i>r</i>
55423.362	0.286 ± 0.008	PTF	<i>r</i>
55480.234	0.184 ± 0.006	PTF	<i>r</i>
55446.370	0.171 ± 0.006	PTF	<i>r</i>
56627.331	0.165 ± 0.018	PTF	<i>r</i>
55205.088	0.135 ± 0.014	PTF	<i>r</i>
55084.360	0.300 ± 0.010	PTF	<i>r</i>
55436.402	0.244 ± 0.010	PTF	<i>r</i>
55457.272	0.299 ± 0.009	PTF	<i>r</i>
56202.197	0.219 ± 0.009	PTF	<i>r</i>
55779.303	0.282 ± 0.008	PTF	<i>r</i>
55445.520	0.170 ± 0.007	PTF	<i>r</i>
55506.351	0.186 ± 0.010	PTF	<i>r</i>

Table S1: Multi-color photometry of M31-2014-DS1 (Continued).

MJD	Flux (mJy)	Instrument	Filter
55429.419	0.264 ± 0.008	PTF	r
55197.083	0.257 ± 0.018	PTF	r
55506.268	0.174 ± 0.009	PTF	r
55429.463	0.267 ± 0.008	PTF	r
55579.197	0.222 ± 0.009	PTF	r
58331.654	< 0.002	ZTF	r
58392.798	0.004 ± 0.001	ZTF	r
58467.947	< 0.011	ZTF	r
58678.700	< 0.004	ZTF	r
58747.804	< 0.002	ZTF	r
58837.716	< 0.007	ZTF	r
58908.036	< 0.008	ZTF	r
59029.181	< 0.004	ZTF	r
59109.081	< 0.003	ZTF	r
59205.556	< 0.005	ZTF	r
59313.438	< 0.010	ZTF	r
59372.351	< 0.004	ZTF	r
59480.794	< 0.004	ZTF	r
59539.573	< 0.014	ZTF	r
59700.192	< 0.017	ZTF	r
59733.505	< 0.004	ZTF	r
59846.143	< 0.004	ZTF	r
59933.688	< 0.007	ZTF	r
60072.128	< 0.011	ZTF	r
60102.157	< 0.004	ZTF	r
60221.421	< 0.004	ZTF	r

Table S1: Multi-color photometry of M31-2014-DS1 (Continued).

MJD	Flux (mJy)	Instrument	Filter
60268.174	< 0.046	ZTF	<i>r</i>
58325.897	0.004 ± 0.001	ZTF	<i>g</i>
58395.616	0.003 ± 0.001	ZTF	<i>g</i>
58496.528	< 0.011	ZTF	<i>g</i>
58704.899	0.002 ± 0.001	ZTF	<i>g</i>
58762.367	0.003 ± 0.001	ZTF	<i>g</i>
58865.832	< 0.006	ZTF	<i>g</i>
59068.172	< 0.001	ZTF	<i>g</i>
59146.807	< 0.004	ZTF	<i>g</i>
59228.958	< 0.006	ZTF	<i>g</i>
59427.416	< 0.004	ZTF	<i>g</i>
59512.400	< 0.005	ZTF	<i>g</i>
59626.165	< 0.042	ZTF	<i>g</i>
59772.890	< 0.006	ZTF	<i>g</i>
59858.624	< 0.004	ZTF	<i>g</i>
59947.290	< 0.007	ZTF	<i>g</i>
60154.428	< 0.005	ZTF	<i>g</i>
60228.151	< 0.004	ZTF	<i>g</i>
56209.318	0.067 ± 0.001	PS1	<i>g</i>
56209.331	0.065 ± 0.001	PS1	<i>g</i>
56570.431	0.091 ± 0.002	PS1	<i>g</i>
56570.440	0.094 ± 0.002	PS1	<i>g</i>
55857.349	0.091 ± 0.002	PS1	<i>g</i>
55857.363	0.094 ± 0.002	PS1	<i>g</i>
55858.291	0.105 ± 0.002	PS1	<i>g</i>
55477.288	0.074 ± 0.001	PS1	<i>g</i>

Table S1: Multi-color photometry of M31-2014-DS1 (Continued).

MJD	Flux (mJy)	Instrument	Filter
55477.301	0.079 ± 0.002	PS1	<i>g</i>
55448.556	0.089 ± 0.002	PS1	<i>g</i>
55448.567	0.097 ± 0.002	PS1	<i>g</i>
56205.343	0.129 ± 0.002	PS1	<i>r</i>
56205.355	0.123 ± 0.002	PS1	<i>r</i>
56599.225	0.318 ± 0.003	PS1	<i>r</i>
56226.317	0.098 ± 0.003	PS1	<i>r</i>
56226.328	0.101 ± 0.003	PS1	<i>r</i>
55857.376	0.182 ± 0.002	PS1	<i>r</i>
55857.388	0.183 ± 0.002	PS1	<i>r</i>
55174.317	0.381 ± 0.003	PS1	<i>r</i>
55174.318	0.379 ± 0.003	PS1	<i>r</i>
55485.290	0.148 ± 0.002	PS1	<i>r</i>
55485.302	0.140 ± 0.003	PS1	<i>r</i>
56226.326	0.104 ± 0.003	PS1	<i>r</i>
56226.316	0.101 ± 0.002	PS1	<i>r</i>
55448.583	0.198 ± 0.002	PS1	<i>r</i>
55448.595	0.194 ± 0.003	PS1	<i>r</i>
56907.435	0.221 ± 0.003	PS1	<i>i</i>
56907.446	0.221 ± 0.003	PS1	<i>i</i>
56907.458	0.221 ± 0.003	PS1	<i>i</i>
56907.469	0.223 ± 0.003	PS1	<i>i</i>
56663.227	0.408 ± 0.005	PS1	<i>i</i>
56663.240	0.393 ± 0.003	PS1	<i>i</i>
56205.436	0.379 ± 0.003	PS1	<i>i</i>
56205.449	0.381 ± 0.003	PS1	<i>i</i>

Table S1: Multi-color photometry of M31-2014-DS1 (Continued).

MJD	Flux (mJy)	Instrument	Filter
56589.450	0.431 ± 0.003	PS1	<i>i</i>
56589.462	0.432 ± 0.003	PS1	<i>i</i>
56641.284	0.452 ± 0.003	PS1	<i>i</i>
56641.296	0.452 ± 0.004	PS1	<i>i</i>
56224.314	0.347 ± 0.003	PS1	<i>i</i>
56224.327	0.335 ± 0.003	PS1	<i>i</i>
55850.468	0.364 ± 0.003	PS1	<i>i</i>
55850.481	0.376 ± 0.003	PS1	<i>i</i>
55486.274	0.356 ± 0.003	PS1	<i>i</i>
55486.286	0.342 ± 0.007	PS1	<i>i</i>
56224.326	0.321 ± 0.003	PS1	<i>i</i>
56224.314	0.330 ± 0.003	PS1	<i>i</i>
55457.543	0.501 ± 0.004	PS1	<i>i</i>
55457.574	0.463 ± 0.004	PS1	<i>i</i>
55962.225	0.686 ± 0.006	PS1	<i>z</i>
55962.236	0.657 ± 0.005	PS1	<i>z</i>
56170.478	0.567 ± 0.006	PS1	<i>z</i>
56170.490	0.558 ± 0.006	PS1	<i>z</i>
56477.598	0.578 ± 0.003	PS1	<i>z</i>
56484.585	0.561 ± 0.006	PS1	<i>z</i>
55563.312	0.719 ± 0.007	PS1	<i>z</i>
55760.573	0.678 ± 0.005	PS1	<i>z</i>
55760.585	0.664 ± 0.005	PS1	<i>z</i>
56637.214	0.568 ± 0.005	PS1	<i>z</i>
55400.602	0.457 ± 0.070	PS1	<i>z</i>
55402.483	0.553 ± 0.006	PS1	<i>z</i>

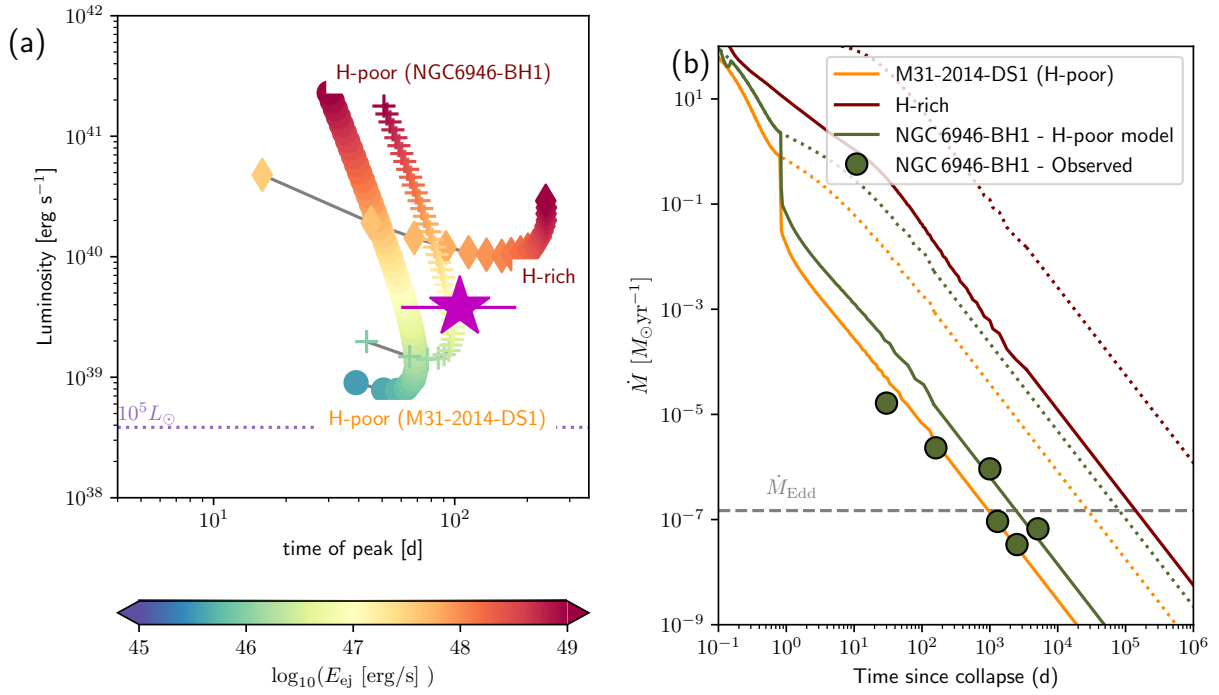


Figure S10: The predicted outburst properties and late-time mass fallback evolution for the model for NGC 6946-BH1, compared to the H-poor and H-rich models for M31-2014-DS1.

(a) The luminosity and timescale of transients powered by H-recombination as a function of shock energy (as in Figure 4) for the favored H-poor model for M31-2014-DS1, the H-rich model for the same object and the progenitor model for NGC 6946-BH1. The magenta star shows the observed luminosity and duration of the NGC 6946-BH1 outburst. (b) The evolution of the mass fall-back rate for the same three models in (a), with dotted lines showing the case for complete accretion and solid lines showing the case accounting for the angular momentum barrier (as in Figure S6). For comparison, we show the observed bolometric light curve of NGC 6946-BH1 from the time of outburst to recent JWST observations (42, 45, 47), converting luminosity into effective mass accretion rate assuming a radiative efficiency of $\eta = 0.05$.

Table S1: Multi-color photometry of M31-2014-DS1 (Continued).

MJD	Flux (mJy)	Instrument	Filter
55402.495	0.505 ± 0.008	PS1	z
56500.602	0.469 ± 0.006	PS1	z
56500.590	0.465 ± 0.007	PS1	z
56867.633	0.550 ± 0.010	PS1	y
55937.201	0.643 ± 0.010	PS1	y
55937.213	0.662 ± 0.009	PS1	y
56526.529	0.614 ± 0.010	PS1	y
55562.295	0.126 ± 0.009	PS1	y
56643.196	0.608 ± 0.009	PS1	y
55378.594	0.687 ± 0.010	PS1	y
55378.605	0.664 ± 0.010	PS1	y
56526.513	0.586 ± 0.009	PS1	y

Table S2: Archival space-based photometry of M31-2014-DS1 from HST and SST. Error bars are provided at 1σ confidence for epochs of detection, and 5σ upper limits are denoted otherwise.

Epoch	Filter	AB Mag	Instrument
2012	F110W	16.86 ± 0.05	HST/WFC3-IR
2012	F160W	16.83 ± 0.05	HST/WFC3-IR
2012	F475W	19.15 ± 0.05	HST/ACS
2012	F814W	17.05 ± 0.10	HST/ACS
2012	F336W	23.25 ± 0.10	HST/WFC3-UVIS
2012	F275W	> 26.18	HST/WFC3-UVIS
2012	Channel 1 ($3.6 \mu\text{m}$)	16.37 ± 0.01	SST/IRAC
2012	Channel 2 ($4.5 \mu\text{m}$)	16.47 ± 0.01	SST/IRAC
2012	Channel 3 ($5.8 \mu\text{m}$)	16.05 ± 0.01	SST/IRAC
2012	Channel 4 ($8.0 \mu\text{m}$)	15.95 ± 0.01	SST/IRAC
2012	Channel 1 ($24.0 \mu\text{m}$)	15.69 ± 0.10	SST/MIPS
2022	F606W	> 28.48	HST/WFC3-UVIS
2022	F814W	27.30 ± 0.23	HST/WFC3-UVIS